Key Points:

- A case study reveals that refraction results in a 25% increase in gravity wave momentum flux (GWMF)
- Including refraction dynamics affects the location of GWMF deposition
- Refraction is prominent in strong wind gradients (i.e., displaced vortex conditions)

Correspondence to:
M. Geldenhuys,
m.geldenhuys@fz-juelich.de;
markusgeld@gmail.com

Author Contributions:
Conceptualization: M. Geldenhuys
Formal analysis: M. Geldenhuys
Investigation: M. Geldenhuys
Methodology: M. Geldenhuys
Validation: M. Geldenhuys
Visualization: M. Geldenhuys
Writing – original draft: M. Geldenhuys
Writing – review & editing: M. Geldenhuys

Observations of Gravity Wave Refraction and Its Causes and Consequences

M. Geldenhuys[1,2] , **B. Kaifler[3]** , **P. Preusse[1]**, **J. Ungermann[1,4]** , **P. Alexander[5]** , **L. Krasauskas[1]** , **S. Rhode[1]** , **W. Woiwode[6]** , **M. Ern[1]** , **M. Rapp[3]** , and **M. Riese[1]**

[1]Forschungszentrum Jülich, Institute of Energy and Climate Research, Jülich, Germany, [2]South African Weather Service, Pretoria, South Africa, [3]Deutsches Zentrum für Luft- und Raumfahrt, Institut für Physik der Atmosphäre, Oberpfaffenhofen, Germany, [4]JARA, Forschungszentrum Jülich GmbH, Jülich, Germany, [5]Instituto de Física de Buenos Aires, CONICET, Buenos Aires, Argentina, [6]Karlsruhe Institute of Technology, Institute of Meteorology and Climate Research, Karlsruhe, Germany

Abstract Horizontal gravity wave (GW) refraction was observed around the Andes and Drake Passage during the SouthTRAC campaign. GWs interact with the background wind through refraction and dissipation. This interaction helps to drive midatmospheric circulations and slows down the polar vortex by taking GW momentum flux (GWMF) from one location to another. The SouthTRAC campaign was composed to gain improved understanding of the propagation and dissipation of GWs. This study uses observational data from this campaign collected by the German High Altitude Long Range research aircraft on 12 September 2019. During the campaign a minor sudden stratospheric warming in the southern hemisphere occurred, which heavily influenced GW propagation and refraction and thus also the location and amount of GWMF deposition. Observations include measurements from below the aircraft by Gimballed Limb Observer for Radiance Imaging of the Atmosphere and above the aircraft by Airborne Lidar for the Middle Atmosphere. Refraction is identified in two different GW packets as low as ≈ 4 km and as high as 58 km. One GW packet of orographic origin and one of nonorographic origin is used to investigate refraction. Observations are supplemented by the Gravity-wave Regional Or Global Ray Tracer, a simplified mountain wave model, ERA5 data and high-resolution (3 km) WRF data. Contrary to some previous studies we find that refraction makes a noteworthy contribution in the amount and the location of GWMF deposition. This case study highlights the importance of refraction and provides compelling arguments that models should account for this.

Plain Language Summary Gravity waves (GWs) are very important for models to reproduce a midatmospheric circulations. But the fact is that models oversimplify the GW physics which results in GWs being underrepresented in models. GW refraction is one of the processes not captured by the physics in model parameterization schemes. This article uses high-resolution observations from the SouthTRAC campaign to show how GWs refract and highlight the importance there-of. This case study shows a 25% increase in the GWMF during propagation. The increase in momentum flux is linked to refraction which results in a shortening in the GW horizontal wavelength. This article shows that refraction is important for the amount as well as the location of GWMF deposition. This case study highlights the importance of refraction and provides compelling arguments that models should account for this.

1. Introduction

Gravity wave momentum flux (GWMF) and its distribution around 60°S recently became a subject of debate (e.g., Ern et al., 2017; Garcia et al., 2017; Geller et al., 2013; Hindley et al., 2020; McLandress et al., 2012; Plougonven et al., 2020). At formation, the GW takes energy from the mean flow and obtains a GWMF, which changes with wave dissipation (Plougonven et al., 2020) and refraction (Hasha et al., 2008). Refraction in the horizontal is the process whereby a GW phase front changes in orientation. Such changes in orientation are linked with changes in the wavelength in the *x*-direction and *y*-direction (Durran, 2009), which has been shown to have important implications for GW propagation (e.g., Dunkerton & Butchart, 1984; Ehard et al., 2017; Sato et al., 2009). A literature survey shows a very small amount of papers on GW refraction compared to GW dissipation and GW breaking. This indicates that a large portion of the academic effort does not include refraction. This article uses high-resolution observational data from the lower troposphere to the lower mesosphere to quantify refraction and show the importance there-of for wave-mean flow interaction.

GWs exist throughout the atmosphere, over a broad range of spatial and temporal scales (Fritts & Alexander, 2003). The larger part of the GW spectrum (>50 km) helps drive stratospheric and mesospheric circulations (Holton, 2004). The slowdown of the stratospheric polar vortex is also affected by GWs (Fritts & Alexander, 2003, and references there in). These two processes affect surface weather over time scales from a few weeks to years (e.g., Kidston et al., 2015; Lim et al., 2019; Polichtchouk et al., 2018a, 2018b). These GWs affect the mean flow by taking momentum flux from one location to deposit at another (Alexander et al., 2010; McLandress, 1998).

Models heavily rely on parameterization schemes to achieve a meaningful GWMF. A GW with a long horizontal wavelength can propagate large horizontal distances from its source (Geldenhuys et al., 2021; Krisch et al., 2017). Modeling this requires complex physics and processes to represent the GW drag amount and location (Plougonven et al., 2020). However, models need to simplify this due to computational constraints and confine all nonresolved GWs to their source column parameterization schemes.

The disagreement between observations and models has created a debate amongst the scientific community (e.g., de la Camara et al., 2016; Garcia et al., 2017; McLandress et al., 2012). McLandress et al. (2012) compared model to reanalysis data and found a large amount of GWMF missing at 60°S. This is a direct result of the limitation imposed in the models on the horizontal propagation of GWs. This triggered a number of studies; some reviewed parameterization schemes (e.g., Geldenhuys, 2022b; Plougonven et al., 2020), some increased drag from other known sources (e.g., Garcia et al., 2017; Polichtchouk et al., 2018a, 2018b; Richter et al., 2010), some studies mention islands might be the source (e.g., McLandress et al., 2012), some looked at new sources (e.g., Doernbrack et al., 2021; Geldenhuys et al., 2021) and others used GW intermittency to show increased drag (e.g., de la Camara et al., 2014, 2016). The large number (listed above) of different studies to solve one problem points to three possibilities: (a) the community is uncertain what the solution is, (b) there are a number of improvements required to our model parameterization schemes, or (c) improvements are required in our understanding.

Model reliance on parameterization schemes is reduced with increases in spatial resolution, but for the immediate future we will still need parameterization schemes. One of the widely used reanalysis data sets (ERA5— European Centre for Medium-Range Weather Forecasts (ECMWF) Reanalysis 5th Generation) deposits more than double the parameterized GW drag compared to resolved GW drag during vortex breakdown (Gupta et al., 2021). Most climate models have resolutions 1 order of magnitude less than ERA5 data (which has a grid spacing of 0.3°), thus we can expect a greater amount of parameterized GW drag in them. Recently IFS (the underlying model of ERA5) doubled their vertical resolution and still the model required a GW parameterization scheme (Lang et al., 2021). This shows how much we rely on parameterization schemes. Dedicated studies (e.g., Geldenhuys, 2022b; Plougonven et al., 2020) and the large effort by the modeling community (e.g., Boeloeni et al., 2021; Kim et al., 2021; Polichtchouk et al., 2018a, 2018b; Sandu et al., 2016) show that parameterizations are still important even though computational developments allow to resolve larger parts of the GW spectrum.

Recently, Plougonven et al. (2020) stated that improved knowledge and developments in models are still required for processes like GW breaking and lateral propagation. Our study suggests that refraction should be added to this list. A GW packet propagates roughly along its phase fronts (Holton, 2004), this implies the orientation and therefore the refraction of the phase fronts are important (Krisch et al., 2017). Additionally, refraction is known to increase or decrease the GWMF of a GW packet (Chen et al., 2005; Hasha et al., 2008), which is another factor not incorporated into the single-column model approach. This poses the curious question of: Why the community is not spending more effort on refraction? One reason can be that Hasha et al. (2008) concluded that GWMF from midfrequency wave changes due to refraction and horizontal propagation is negligible. However, they explicitly stated that a large shortcoming of their study was that they ignored nonorographic GWs and used a low model resolution (T47, or about 2.5°) compared to today's standard. The study by Hasha et al. (2008) was criticized by a commentary (Durran, 2009), who referenced an earlier study of Chen et al. (2005) saying that refraction of high-frequency GWs greatly impact the GWMF on a case-by-case basis. Dunkerton (1984) showed that stationary GWs are refracted and focused into the polar night jet by meridional shear. A modeling study by Sato et al. (2012) with a horizontal resolution of 60 km and vertical resolution of 300 m showed GWs propagate meridionally toward the 60°S polar vortex—stronger wind regions. Several other studies (e.g., Ehard et al., 2017; Preusse et al., 2002, 2009; Sato et al., 2009) looked at refraction or the focusing of GWs into the jet. Sato et al. (2009) state that "reality must be confirmed" by high-resolution observations. Although Ehard et al. (2017) is an observational study which mentions refraction, no observations of refraction were possible with their single

stationary lidar. Observations are required for improved understanding of horizontal propagation, refraction, and how to constrain the GWMF in models. Quantifying the horizontal propagation of mountain waves was one of the principle scientific objectives of the SouthTRAC field campaign.

SouthTRAC was an observational campaign aimed at answering some of the above-mentioned shortcomings. The campaign was carried out in September and November 2019 and was based at the world's GW hotspot, the Southern Andes (Rapp et al., 2021). Rio Grande in Argentina acted as a base, from where seven flights dedicated to GWs were performed. For more information on the campaign, we refer to Rapp et al. (2021) and for flight planning refer to Bauer et al. (2022). The flight discussed here was the first local science flight of the campaign and provided some of the last high propagating GWs of the 2019 winter season (see Section 3.1 for reasons). High-resolution observations of orographic and nonorographic GWs are used to detect refraction from the troposphere to the mesosphere. The observations are combined with model data to reveal what caused the refraction. The consequences of refraction are demonstrated by multiple raytracing experiments and calculating the GWMF along the ray path.

In this article, we diagnose refraction from our observations as a quantified change in GW orientation in time or with altitude. This entails also a change in the wavelength in the *x*-direction and *y*-direction (as well as total wavelength as shown in Section 4). Section 2 describes the observational data, model data, and tools employed during analysis. Section 3 starts with a synoptic overview followed by a discussion of the GW observations and their sources. Section 4 deals with the causes and consequence of refraction. The final section summarizes the results and highlights the importance of refraction.

2. Data and Methods

2.1. Observational Data

Observational data for this case study include data from the Gimballed Limb Observer for Radiance Imaging of the Atmosphere (GLORIA) and Airborne Lidar for the Middle Atmosphere (ALIMA) instruments both situated onboard the HALO (German High Altitude Long Range) research aircraft. GLORIA can observe 3-D volumes below flight altitude while ALIMA measures vertical profiles of temperature above the aircraft. GLORIA has been used in multiple aircraft campaigns and its corresponding observations are discussed in, e.g., Krisch et al. (2017), Krisch et al. (2018), Woiwode et al. (2018), Höpfner et al. (2019), Krasauskas et al. (2021), and Geldenhuys et al. (2021). ALIMA was flown for the first time in SouthTRAC; however, observations from CORAL (a ground-based version of ALIMA) are discussed in, e.g., Reichert et al. (2019), Kaifler et al. (2020), Kaifler and Kaifler (2021), and Reichert et al. (2021).

2.1.1. GLORIA Instrument and Retrieval Description

GLORIA is an infrared spectrometer that measures spectra between 780 and 1,400 cm^{-1} (Friedl-Vallon et al., 2014; Riese et al., 2014). The instrument contains a Michelson interferometer and a 2-D infrared detector array. In the setup during SouthTRAC, 48×128 pixels (horizontal $\times$ vertical) of the detector array were used for limb sampling. During each interferometer sweep, each pixel records a full interferogram. The interferograms are transformed to spectra, and the spectra within pixel rows are binned. The tangent point is the point closest to the surface of the earth where the density is the highest. The tangent point generally corresponds to the maximum signal, since the weighting function of the radiation transport has a maximum here in the optically thin case. This is a consequence of the spherical measurement geometry and the exponentially decreasing atmospheric density with altitude. The tangent point generally is seen as a region of trust in our tomographic retrievals.

GLORIA (Friedl-Vallon et al., 2014; Riese et al., 2014) is located in the belly pod of HALO and looks to the right with regard to flight direction. The field of view extends 4.1° in the vertical and the gimbal frame allows the instrument to pan from right-backwards (135° to aircraft heading) to right-forwards (45°). The vertical field of view allows a viewing depth from ≈5 km to just above flight altitude. Below ≈5 km, the atmosphere becomes too optically thick for infrared limb viewing measurements as the signal becomes saturated by spectral signatures of tropospheric trace gases, clouds, and aerosols. The measured radiance spectra can be analyzed for signals of CO_2, O_3, H_2O, NH_3, $ClONO_2$, HNO_3, and PAN—peroxyacetyl nitrate, among others.

In this article, we use emission lines of the CO_2 band at 936.8–938.6, 939.2–941.0, and 942.2–944.2 cm^{-1} to retrieve temperature. The forward model for the retrieval used a spectral resolution (of 0.2 cm^{-1}) similar to the

GLORIA spectral sampling. The data presented in this article were obtained by panning the instrument from 49° to 129° in 11 steps of 8°.

The GLORIA data were processed into a 1-D retrieval and a 3-D data set. A 1-D retrieval converts single radiance profiles into temperature profiles by assuming a horizontally homogeneous atmosphere. A 1-D retrieval consists of a temperature signal that was averaged over each row of detector array for each respective line-of-sight. The retrieved result of each detector row average is represented by its tangent point along the line-of-sight. This produces 11 different 1-D retrievals from each of the azimuth angles. The GW perturbation was extracted from the 1-D retrieval by subtracting a smoothed ECMWF temperature, which is also the a priori of the retrieval. To obtain a 3-D data set, tomography is required. Two types of tomography exist, full-angle and limited-angle tomography. Full-angle tomography can take place where the airmass is observed from all sides by a circular flight path (e.g., Krasauskas et al., 2021; Krisch et al., 2017). Limited-angle tomography is obtained from straight flight legs (e.g., Geldenhuys et al., 2021; Krisch et al., 2018). The panning ability allows GLORIA to observe a single airmass from different angles. This allows us to reproduce a 3-D atmosphere (for details on this please refer to e.g., Ungermann et al. (2011), Kaufmann et al. (2015), Krisch et al. (2018), and Krasauskas et al. (2019)). The data were processed using the GloriPy (Kleinert et al., 2014) and JURASSIC2 (Juelich Rapid Spectral Simulation Code version 2; Ungermann et al., 2010) software packages. Similar to Geldenhuys et al. (2021) and Krasauskas et al. (2021), the retrieval used the Laplacian regularization with a Delaunay triangulation-based, irregular grid-capable discretization. The GW perturbation was extracted from the 3-D retrieval by subtracting a smoothed retrieval. The smoothed retrieval was created by applying a third-order polynomial smoothing in the x-direction and y-direction with 51-point smoothing (this should exclude all horizontal wavelengths shorter than 640 km) and a fourth-order polynomial in the z-direction with 11-point smoothing.

For data analysis, a 3-D data set is normally better than a 1-D or 2-D data set. This also applies to GLORIA data and the 3-D data set is the preferred data set as it provides the full 3-D wave vector. However, the flight pattern in this case study only allowed limited-angle tomography, which can marginally affect the orientation of GWs (see Krisch et al., 2018; this is not a problem for full-angle tomography). Provided that the orientation in the 3-D data set might be affected, the 1-D retrieval is expected to capture the GW orientation similarly or better.

2.1.2. ALIMA

ALIMA measures the atmospheric density profile from which temperature is calculated (Rapp et al., 2021). ALIMA is an iron resonance and Rayleigh lidar; however, during the SouthTRAC campaign, only the Rayleigh lidar was installed. Within the HALO body there is an optical window, which allows ALIMA to look upwards. Under ideal conditions, ALIMA measures from 2 km above flight altitude up to 80 km by Rayleigh scattering.

Measuring up to 80 km requires a strong initial pulse and multiple fine-tuned detectors. ALIMA provides an initial pulse at 532 nm and receives backscatter by a telescope 48 cm in diameter (Rapp et al., 2021). The detected backscatter has a large dynamic range. Thus, ALIMA uses three detectors with different sensitivities that are optimized for the near, mid, and far region. A mechanical chopper blocks the intense backscattered light originating within 4 km above the aircraft in order to prevent overloading of the detectors. The mid and far detectors are gated relative to the opening of the chopper to avoid saturation.

Following Hauchecorne and Chanin (1980), the lidar profile from each detector is converted to a temperature profile by hydrostatic downward integration in steps of 100 m. This requires a top of profile temperature, which is taken from SABER satellite data. The top of profile temperature of the lower profiles is taken from the above profile. The three profiles are then merged into a single profile covering the whole altitude range (Kaifler & Kaifler, 2021). At the top of the profile, the error can be large, but since pressure increases exponentially downwards, the error similarly decreases exponentially downwards. The error decreases from 6.5 K above 70 km to 2.9 K between 60 and 70 km to 0.9 K below 60 km (Rapp et al., 2021). Temperature data used in this manuscript had a 1-min resolution, which roughly equates to ≈15 km resolution along the flight direction.

To extract GW perturbations from ALIMA a 30 min running mean temperature is subtracted. Removing the background temperature reveals a complex GW structure exhibiting GWs of different scales and different propagation directions. Wavelet analysis was used to further analyze this complex interference pattern. Wavelet analysis has been applied to lidar data before to separate GWs of different orientations (Kaifler et al., 2017). Assuming nonstationarity on the straight flight legs a 2-D Morlet continuous wavelet transform (e.g., Torrence & Compo, 1998) was computed according to Chen and Chu (2017), using a Morlet oscillation parameter (k factor) of $2/\pi$. We found

a discretization starting at a spatial scale of 40 km while using 20 spatial and 30 angular scales sufficient in order to separate different slants of GW phase fronts. By making the assumption that the GWs propagate against the ERA5 reanalysis wind we determine upward and downward propagating GWs. It is known that that GWs can propagate with or against the wind and can be partly diagnosed depending on the vertical phase slant. We assume the most frequently observed case; propagation against the mean wind. It is assumed that GWs propagating with the wind is rapidly swept out of the observation regime. By making the assumption that the GW wavevector projected onto the wind will point opposite to the ERA5 wind direction we can determine upward and downward propagating GWs depending on the vertical phase slant.

The 2-D Morlet continuous wavelet transform is much better equipped than the fast Fourier transform to deal with nonharmonic waves, but there are still some inherent problems visible in the derived amplitudes. An amplitude signal of an upward (downward) propagating nonharmonic GW will leak to the downward (upward) propagating GW, lowering the "real" temperature amplitude of the GW. For this reason, all temperature amplitudes were determined using temperature perturbation components before application of the continuous wavelet transform.

2.2. Model and Reanalysis Data

2.2.1. Mountain Wave Model

The mountain wave model is a tool to estimate mountain wave activity. Mountain wave activity is estimated by a three-step process: ridge identification, GW characteristics determination, and GROGRAT raytracing. The model itself follows the original approach of Bacmeister et al. (1994), but differs in a key aspect of the ridge detection method. Briefly described, the mountain wave model reduces a given set of topography (ETOPO1 1Arc-Minute Global Relief Model (Amante & Eakins, 2009); the domain in this instance was 32°S 80°W to 70°S 50°W) to a set of possible ridges by applying a Gaussian bandpass filter to single out the scales of interest and performing a probabilistic Hough transformation. This provides lines representing possible corresponding positions, lengths, and orientations of mountain ridges. Afterward the mountain wave parameters are estimated by fitting idealized (Gaussian shaped) ridges to the bandpass filtered topography for each of these lines. From this, a horizontal wavelength as well as displacement amplitude is estimated. The horizontal wavelength is determined by multiplying the ridge width by a fixed factor. The displacement amplitude reflects the height of the barrier. The forcing wavelength, amplitude, and orientation of the GWs will always be the same, as the mountains do not change. By passing these GW characteristics to the GROGRAT raytracer hourly, the model can predict the time development of the mountain waves. For information regarding the background data for input into GROGRAT, see Section 2.2.3.

2.2.2. WRF (Weather Research and Forecasting) Model Data

A high-resolution WRF model (version 4.2) is used to fill the data gaps when validating the raytracing and ALIMA results (Section 3). Boundary input conditions were supplied every 6 hr at a $0.25 \times 0.25°$ resolution from the Global Data Assimilation System (GDAS) from the National Centres for Environmental Prediction (NCEP). The WRF model was nested twice to produce a 9 km and ultimately a 3 km horizontal grid point distance. Vertical resolution was 0.5 km. The data extend from the surface to 42 km with a 10 km sponge. Only data below the sponge layer (32 km) are used in this work. The model spin-up time was 1 day—only data after spin-up time was used.

To separate GWs from the background fields, a 2-D Fast Fourier Transform was used. The spectrum was cut at a horizontal wavelength of 400 km, retaining all longer wavelengths in the background. The GW perturbation field formed the residual after the background field was subtracted from the actual field. Experiments with a 600 km cut-off produced similar GW perturbations.

2.2.3. Reanalysis Data

This article uses ERA5 (European Centre for Medium-Range Weather Forecasts Reanalysis 5th Generation; Hersbach et al., 2020) data on a $0.3° \times 0.3° \times 200$ m grid on geopotential altitudes. Only data for the synoptic discussion are on a pressure grid. To remove the GW component from the background flow, a zonal Fast Fourier Transform was used with a cut-off at zonal wavenumber 12 (Strube et al., 2020), corresponding to 1,900 km. This was followed by a Savitzky-Golay filter (Savitzky & Golay, 1964) in the y-direction and z-direction. In the meridional (y) direction, a third-order polynomial with a 50 point (15° of longitude) smoothing was applied. In the remaining direction (z), a fourth-order polynomial was applied with a 15 point

(3 km) smoothing. The result after smoothing produces the background conditions. Subtracting the smooth background conditions from the original field produces the GW perturbation component. The smooth background fields were visually studied to ensure no GWs signals were left in the field. The smooth background is used as input into the GROGRAT raytracer. The unfiltered horizontal divergence field is used to show the GW field.

2.3. GROGRAT—Gravity-Wave Regional Or Global Ray Tracer

GROGRAT traces the propagation of a GW forward or backward in time. GROGRAT uses the dispersion relation (Eckermann & Marks, 1997; Marks & Eckermann, 1995)

$$\omega^2 = \frac{\left(k^2 + l^2\right)N^2 + f^2\left(m^2 + \frac{1}{4H^2}\right)}{k^2 + l^2 + m^2 + \frac{1}{4H^2}} \tag{1}$$

and the raytracing equations

$$\frac{dk}{dt} = -k\frac{\partial u}{\partial x} - l\frac{\partial v}{\partial x} - \frac{1}{2\omega\Delta}\left[\frac{\partial N}{\partial x}^2\left(k^2 + l^2\right) - \frac{\partial \alpha}{\partial x}^2\left(\omega^2 - f^2\right)\right] \tag{2}$$

$$\frac{dl}{dt} = -k\frac{\partial u}{\partial y} - l\frac{\partial v}{\partial y} - \frac{1}{2\omega\Delta}\left[\frac{\partial N}{\partial y}^2\left(k^2 + l^2\right) - \frac{\partial \alpha}{\partial y}^2\left(\omega^2 - f^2\right)\right] - \frac{f}{\omega\Delta}\frac{\partial f}{\partial y}\left(m^2 + \alpha^2\right) \tag{3}$$

where ω is intrinsic frequency, N is Brünt-Väisälä frequency, f is Coriolis frequency, H is scale height, k, l, m are wavenumbers in x-direction, y-direction, z-direction, u is zonal wind, v is meridional wind, $\Delta = (k^2 + l^2 + m^2 + \alpha^2)$, $\alpha = \frac{1}{2H_\rho}$, and H_ρ is density scale height. GROGRAT use these equations and ω_{gb}, k, l (where $_{gb}$ indicates ground-based) and location as input to calculate the propagation path of the GW in space and time. Wave action density

$$A \equiv \frac{\bar{E}}{\omega} \tag{4}$$

is conserved along the ray path. Thereby, $\bar{E}$, the total energy transported by the waves, is defined as

$$\bar{E} = \frac{1}{2}\rho\left(\frac{\hat{T}}{T}\right)^2\left(\frac{g}{N}\right)^2\frac{\omega^2}{\omega^2 - f^2} \tag{5}$$

where ρ is density, g is the gravity constant, $\hat{T}$ is temperature amplitude, and T is temperature. In addition, wave amplitude growth is limited by saturation amplitudes calculated using the scheme of Fritts and Rastogi (1985), while turbulent and radiative damping are considered according to Pitteway and Hines (1963) and Zhu (1993). For a detailed mathematical description, refer to Marks and Eckermann (1995), Eckermann and Marks (1997) and references there in.

GROGRAT uses the smoothed ERA5 background wind, temperature, and pressure (Section 2.2.3) that varies in time as input into the raytracing equations. This means that the background conditions influencing the wave vector vary with every time step of ray integration. This forms the 4-D propagation setup, meaning the wave can propagate in time, latitude, longitude, and altitude direction. The propagation physics is complete as far as WKB (Wentzel-Kramers-Brillouin approximation; Hertzog et al., 2001; Marks & Eckermann, 1995) allows and comprises in particular horizontal propagation and refraction (similar to the setup used in Krisch et al. (2017), Krisch et al. (2020), Geldenhuys et al. (2021), Strube et al. (2021)). GROGRAT backtracing is valuable for finding sources, but GROGRAT cannot directly diagnose sources. Source identification along the backtracing ray path is left to the user to find at any point along the ray path. In this paper, alternative 3-D and 1-D propagation setups are used to compare to the 4-D propagation results. The 3-D propagation setup assumes the background constant with time and uses a single snapshot to propagate the GWs. The 1-D setup represent conditions when horizontal propagation and refraction are both disabled by setting the horizontal phase speed, $\frac{dk}{dt}$ and $\frac{dl}{dt}$ (Equations 2 and 3) to 0. This is analogous to a 1-D, single-column, parameterization scheme employed in a general circulation model.
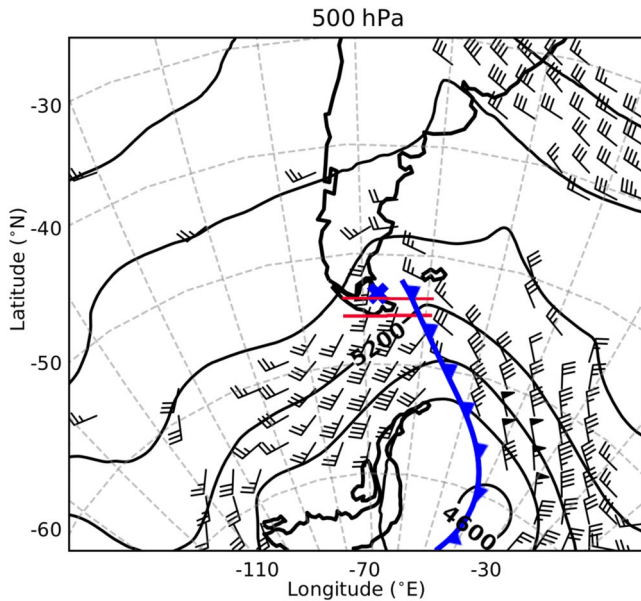
Figure 1. Synoptic situation in the midtroposphere at 500 hPa (corresponding to ~5-km altitude) on 12 September at 03:00 as indicated by ERA5. Black lines show geopotential height lines. Wind barbs only show wind where the total wind speed exceed 20 m s⁻¹. A short barb indicates 5 m s⁻¹, a long barb 10 m s⁻¹ and a triangle 50 m s⁻¹. Note the Rossby wave with the cold front (blue line) directly downstream of Patagonia. The blue cross indicates the take-off location (Rio Grande) and the red lines over the southern tip of South America show the parallel racetrack legs used in the Gimballed Limb Observer for Radiance Imaging of the Atmosphere and Airborne Lidar for the Middle Atmosphere retrievals.

3. Synoptic Overview and Refraction Observation

This section introduces the information required for Section 4. To understand the cause and consequence of refraction, the readers need to acquaint themself with the background wind conditions (synoptic discussion) and the GW characteristics (GW observations) discussed in this section. The stratosphere was heavily influenced by an anomalously strange event called a sudden stratospheric warming. To understand GW propagation, this event needs to be covered in some detail. The background wind conditions allowed the GWs to propagate long horizontal distances while causing refraction of the GW phase fronts. This section also describes the very first atmospheric observations of GW refraction. We provide evidence of refraction in the troposphere and the stratosphere/lower mesosphere, and we employ GROGRAT to demonstrate how these GWs refract and propagate long horizontal distances from their sources. This builds toward an experiment in Section 4 to show the impacts of refraction on GW propagation paths, momentum flux amplitudes, and momentum flux deposition locations.

3.1. Synoptic Situation

GW refraction depends on the background wind (see Section 4 for an in-depth discussion); hence, a discussion of the synoptic situation in the troposphere and stratosphere is important. The research flight took off on 11 September 2019 at 23:00 UTC and landed on 12 September shortly before 07:00 UTC. All dates provided in this article pertain to the year 2019 (unless explicitly stated otherwise) and all times are in UTC. The observations discussed in this article were performed between 03:30 and 06:30 when the racetrack (a flight pattern consisting of two legs parallel to one another) was flown. Observations used in this article are from the long parallel legs of the racetrack (red lines in Figure 1). The southern leg was flown first from east to west followed by the northern leg from west to east. We choose 03:00 on 12 September to be representative for the synoptic situation of the racetrack. At 500 hPa over the Drake Passage, Figure 1 shows south-westerly winds behind the blue line and north-westerly winds ahead of the blue line. Such a wave-like pattern in the tropospheric polar front jet is typical of a Rossby wave.

The cold front (blue line in Figure 1) passed over Rio Grande ≈5 hr before flight take-off. The cold front is situated in a well developed Rossby wave at 500 hPa. Behind the cold front cold stable air is advected onshore by a ridging high-pressure system. This creates (and is shown in Figure 1) south-south-westerly flow over the southernmost tip of Patagonia, veering to southwest (at 50°S), west-southwest (at 45°S), and west (at 40°S) in a northwards direction along the Andes mountain range. The stable conditions with wind flow nearly perpendicular (within 30°) across the mountains (Geldenhuys et al., 2019; ICAO, 2005) creates prime conditions for a whole spectrum of different orientation GWs entering the observation regime (e.g., Kogure et al., 2020; Vadas & Becker, 2019). The narrow mountains on the tip of Patagonia are expected to form shorter horizontal wavelengths. The broad Andes ridge to the north is expected to excite long horizontal wavelengths with possible shorter waves coming from the side ridges leading up to the main ridge (Van der Mescht & Geldenhuys, 2019). All of these GWs are expected to superimpose and create a rather complex interference pattern.

Polar stratospheric clouds formed presumably in the GWs coming from the broad main ridge. The clouds were observed in the racetrack at 23-km altitude by ALIMA (Dörnbrack et al., 2020). Enhanced backscatter from the clouds means that ALIMA temperature measurements can only be used above this altitude or need to be interpolated through the cloud layer. The polar stratospheric clouds extended unusually far north. This was attributed to a displaced stratospheric polar vortex.

The most significant event in the atmospheric region under consideration was a sudden stratospheric warming (Shen et al., 2020). Figure 2 shows a displaced vortex which led to the minor sudden stratospheric warming. This sudden stratospheric warming was forced by a bottom-up mechanism: an anomalously strong wavenumber
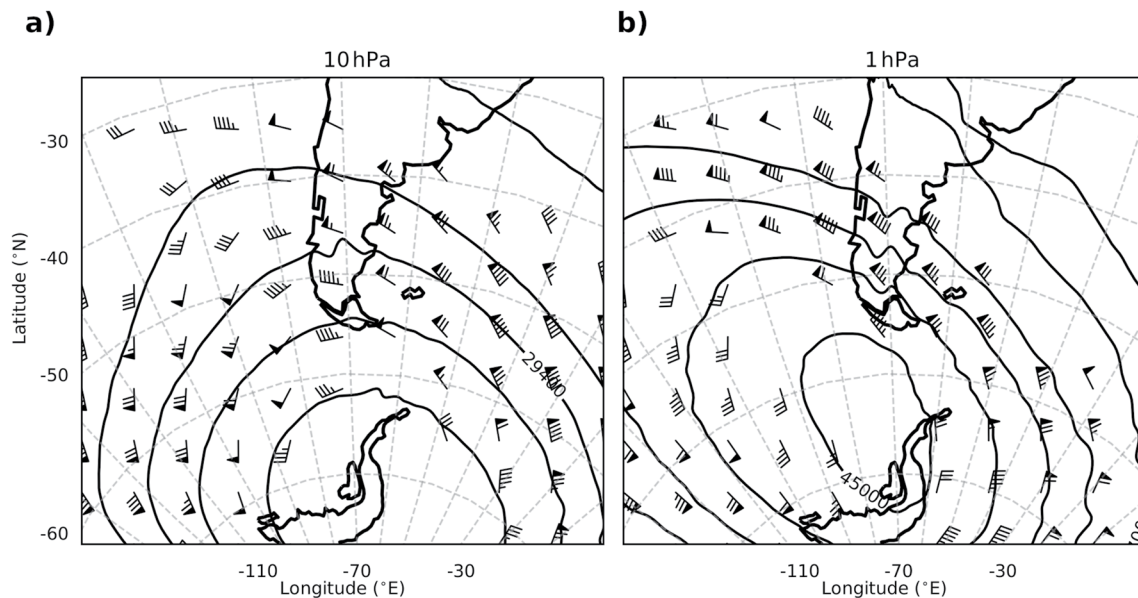
a)   b)

Figure 2. Stratospheric synoptic situation at 10 hPa (a) and 1 hPa (b) on 12 September at 03:00 as indicated by ERA5 (corresponding to ~30-km and 50-km altitudes). Black lines and wind barbs are similar to Figure 1. Note the displaced polar vortex with its center located at 70°S 60°W at 10 hPa and 65°S 75°W at 1 hPa.

1 activity propagating upwards from the troposphere. The strong wavenumber 1 activity was in turn forced by anomalously strong convection over the Pacific Ocean. The sudden stratospheric warming caused a rapidly weakening polar vortex with temperatures increasing rapidly from above to below. Both the weakening in the wind and the strong change in temperature is unfavorable for GW propagation and cause GW dissipation or the trapping of GWs. Both of these act as a lid to restrict the GW activity moving upwards (e.g., Kogure et al., 2021; Kohma et al., 2021).

The slowdown in the 10 hPa zonal average winds appeared in the first few days of September; using MERRA-2 data. MERRA-2 (Modern-Era Retrospective analysis for Research and Applications—Gelaro et al., 2017) data are used as it assimilates MLS (Microwave Limb Sounder) satellite data, which makes it a more trustworthy data set in the upper stratosphere and lower mesosphere (Ern et al., 2021). By 11 September, the slowdown had merely started and still allowed GW propagation to vortex altitudes. Figure 2 confirms this by the evident strong westerly winds still in ERA5. The location of the polar vortex creates a large amount of wind speed shear and directional shear. The shear is expected to form prime conditions for refraction where a GW with a wave vector previously pointing directly into the wind now changes its orientation due to wind shear.

3.2. GW Observations and Modeling: Tropospheric and Lower Stratospheric

The viewing geometry of GLORIA allows tropospheric and lower stratospheric observations. The southern leg of the racetrack (Figure 1) was used in the GLORIA retrieval and was flown from east to west at 13.5 km. This subsection illustrates the first observation of GW refraction from 8 to 13.5 km. The 3-D and 1-D discussion which follows provides the GW input conditions for the raytracing experiments in Section 4. GROGRAT is used to indicate that the source of the observed GWs are the mountains and that GROGRAT is still trustworthy as it resolves the physics of the refracting GW. Finally, this section includes a small part on comparing the GLORIA observed GWs placed into the GROGRAT raytracer with ALIMA and WRF. This comparison is made purely to put trust in the GROGRAT raytracer, which is used extensively in the next section.

3.2.1. GLORIA Observations: 3-D

The 3-D GLORIA temperature field is obtained from a 3-D tomographic retrieval. Figure 3 shows a horizontal cross-section through the tomographic retrieval at 10 km. The retrieval reveals short horizontal wavelength GWs in the lee of the south western most tip of Patagonia. The horizontal cut in Figure 3 shows two distinct GW orientations. The first is aligned west-east (wave vector pointing toward 180° in the traditional coordinate system) and the second from northwest to southeast (230°). Taking the GLORIA viewing geometry into consideration,
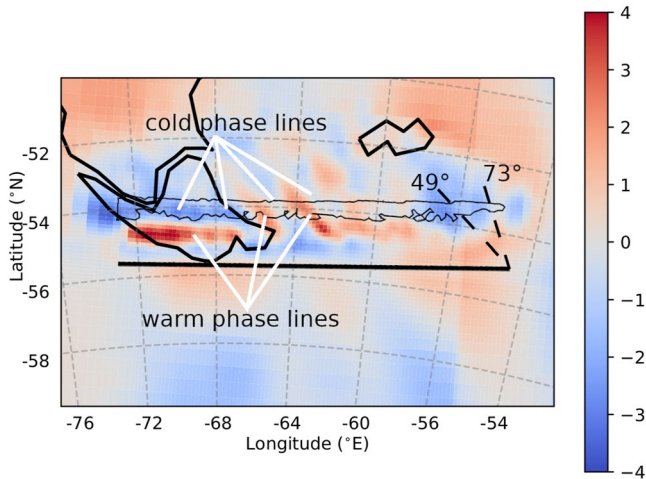
Figure 3. Temperature perturbation component at 10-km altitude of the Gimballed Limb Observer for Radiance Imaging of the Atmosphere (GLORIA) tomographic field. The retrieval was computed using data only from the southern leg (thick black line). Using both the northern and southern legs in a combined tomographic retrieval created artifacts due to nonsymmetrical tangent point distribution. A retrieval using only the northern leg produced a gravity wave (GW) field similar to the southern leg. Black solid lines indicate the Patagonia coastline and the straight white solid lines point to different phase fronts. The region encircled by the thin black line indicates our tangent point region for this altitude, which is our region of trust (Section 2.1.1). The dashed black lines indicate the maximum and minimum GLORIA line-of-sight angle discussed in Figure 4.

we theoretically have less trust in the west-east orientated feature. The viewing angles of GLORIA are aligned across the west-east orientated phase fronts.

If the line-of-sight spans across a positive and a negative region, the signal will be an averaged value of the warm and cold regions. The amount that each feature contribute depends on the density. The densest part will have the most molecules, radiating the most energy. This means the warm and the cold phase fronts average out to have a weak signal, i.e., no retrievable GW. Considering this, we are tempted to classify these structures parallel to the flight path (the westernmost indicated warm front in Figure 3) as artifacts, however, in the mountain wave model (Section 2.2.1) and the high-resolution WRF model (Sections 2.2.2 and 3.2.3) this structure also exists. This adds trust to the retrieval process (and the complex physics and mathematics behind it), when the result is better than what simplified physics dictate it should be.

The second GW orientation is aligned northwest to southeast. Horizontal cuts at different altitudes similar to Figure 3 and a vertical cut perpendicular through the GW phase fronts reveal a horizontal wavelength of 116 km, vertical wavelength of 4.4 km, amplitude of ≈3 K and an orientation of 230°. Krisch et al. (2018) found that limited-angle tomography (method used to produce the 3-D retrieval while flying on straight legs) enhances the uncertainty/error of the phase-front orientation. Considering that orientation is important in a refraction study, we complement the orientation results with the 1-D retrieval.

3.2.2. GLORIA Observations: 1-D

A 1-D GLORIA retrieval consists of a retrieved temperature signal for a single line-of-sight. The 1-D data are combined along the aircraft direction of flight to create a 2-D data set. The first dimension represents time and the second altitude. Figure 4 shows that each GLORIA viewing angle observes the GW phase front differently. Where the line-of-sight aligns along the GW phase front a greater signal is obtained, as opposed to looking across the phase fronts at an angle. Looking across a succession of GW phase fronts dampens the wave amplitude in the observed radiance (Preusse et al., 2002). For a specific altitude, the maximum temperature amplitude is reached when the line-of-sight and phase fronts are aligned. The viewing angle of the most pronounced signal is then used for the wave orientation with an error of half a scanning step (4°) as error estimate.

At 8-km altitude, the maximum amplitude in Figure 4 is observed for an angle of 65°. The maximum at 10 km occurs at 57° and at 12 km at 49°. Taking into account the aircraft heading of 268° and subtracting 90° to convert from phase-front orientation to wavevector, we obtain a ground-based orientation of 243° for the 65° viewing angle. Satellite data from GOES (Geostationary Operational Environmental Satellite—not shown) channel 8 to 10 indicate a GW orientation of ≈240° between ≈615 hPa (≈4 km) and 340 hPa (≈8 km), consistent with the lowest GLORIA altitude. Accounting for the fact that amplitudes are maximum at different altitudes for different GLORIA viewing angles, we can conclude that at higher altitudes (Figure 4) the orientation turns anticlockwise to 235° at 10 km (confirming the orientation derived from Figure 3) and <227° at 12 km (GLORIA has no viewing angles lower than 49°, which means the orientation can be lower than 227°). Assuming one wave packet with a fixed orientation at launch, the refraction between 8 and 12 km is at least 16°.

The orientation analysis in Figure 4 provides the first observed evidence of refraction in the troposphere and lower stratosphere. Also, the analysis provides an accurate orientation for GROGRAT raytracing (see next section).

3.2.3. Observations, Raytracing, and WRF Comparison

In this section, the source of the northwest to southeast orientated GW shown in Figure 3 is determined. In addition, GROGRAT is checked for consistency to ALIMA, GLORIA, and WRF before subsequent experiments are conducted in Section 4.2. GROGRAT requires the ground-based frequency as well as the wavelength in
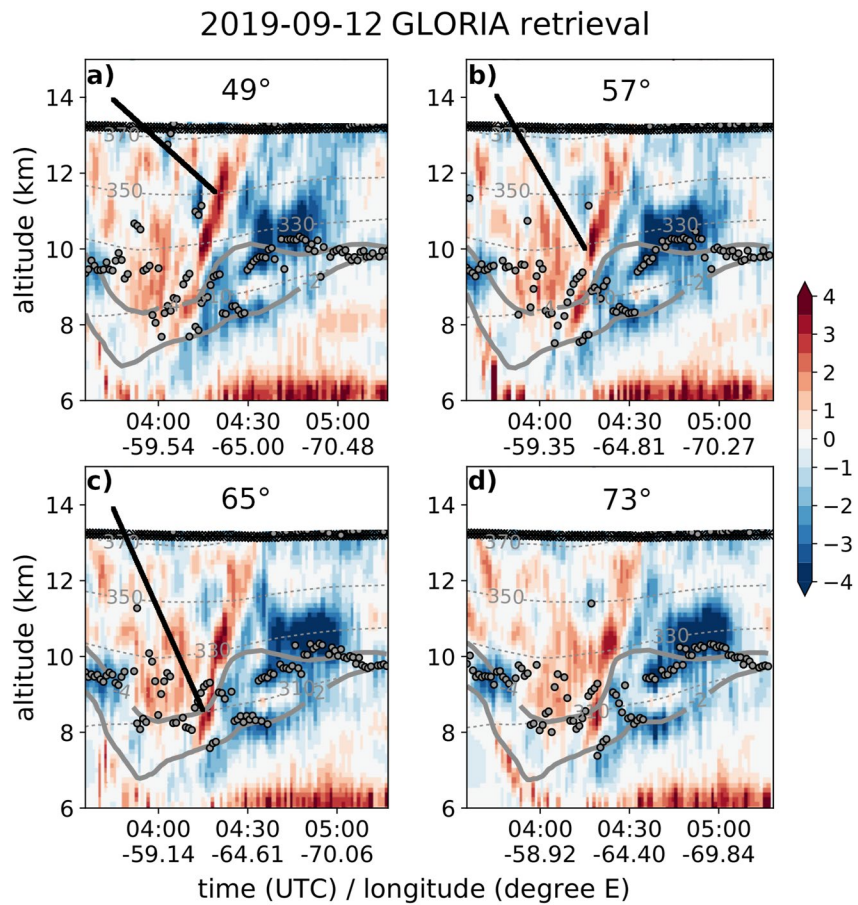
Figure 4. Temperature perturbations (in K) from Gimballed Limb Observer for Radiance Imaging of the Atmosphere 1-D observations for 4 of the 11 azimuth angles (49°, 57°, 65°, and 73°). The red phase front corresponds to the northwest to southeast orientated GWs in Figure 3. The angles are between the observation direction and HALO aircraft heading. Note how the maxima of the warm phase front at fixed altitudes (marked by thick black line) depend on the viewing angle. Flight altitude was at 13.5 km, the thick gray lines indicate dynamic tropopause at −2 and −4 potential vorticity units and the thin dashed gray lines show potential temperature—both extracted from ECMWF analysis data. The dots indicate the suggested thermal tropopause as determined from the retrieval; however, the gravity wave (GW) signature will influence this. Data are valid for the southern leg of the racetrack and longitude values represent tangent point longitude.

the *x*-direction and *y*-(zonal and meridional) direction as input. The ground-based frequency is obtained via the dispersion relation (Equation 1) from the observations (shown in Figure 3 and discussed in Section 3.2.1, while the orientation (or wavevector) is discussed in Section 3.2.2) and ERA5 background winds. To account for the measurement error, the input values are perturbed by 10% to form an ensemble raytrace. The yellow region in Figure 5 shows the ensemble backtrace produces a spread of rays surrounding the south coast of Patagonia. The yellow region includes all but one ensemble member; the perturbation associated with a shorter vertical wavelength propagated to 58.5°S 75.5°W and was neglected in the spread. All ensemble members end in close vicinity in the horizontal and vertical to the coastal mountains (Figure 5). This is a key indicator that the complex mountains on the south coast of Patagonia are the source of the GWs. No indications or indexes showed anything for nonorographic sources along the ray path. GLORIA observed the GWs ≈5 hr after formation. Figure 5 shows that the GROGRAT suggested horizontal wavelength, vertical wavelength, and phase orientation agrees well with the ERA5 data. The consistency builds trust in the features seen in observations, GROGRAT and ERA5.

The forward raytrace shown in Figure 6 uses the GLORIA observed GW (shown in Figures 3 and 4) as input and is compared to ALIMA for further verification. The ray remains below the ALIMA observational range and reaches ALIMA observational altitudes south of the racetrack (Figure 6). The ray takes ≈3 hr to propagate from the observation altitude to 27 km. Time wise this makes the raytrace directly comparable to the WRF data on 12 September 06:00. The ALIMA southern leg was flown east to west between 03:30 and 05:20 and hence 40 min
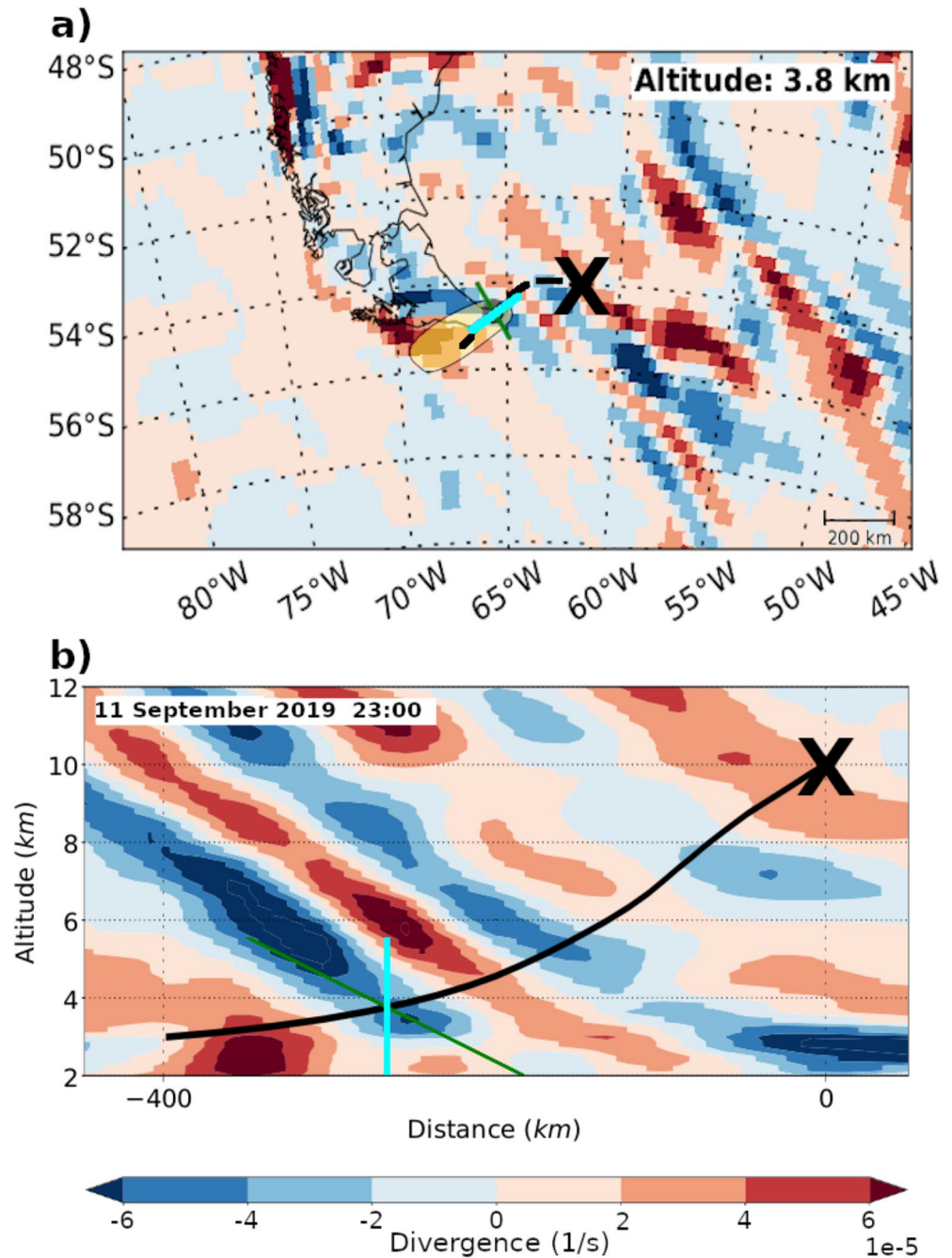
Figure 5. GROGRAT backtrace using Gimballed Limb Observer for Radiance Imaging of the Atmosphere observations as input overlaid on horizontal wind divergence from ERA5. The raytracing starts on 12 September at 03:00 at 10 km and traces back ≈5 hr. Both panels a and b are valid for 23:00, 4 hr before observation. Panel a shows a horizontal cross-section with the ray as a dashed line and ERA5 divergence at 3.8 km. The yellow transparent region surrounding the end of the ray shows the spread of the ensemble members. The thin black line represents the coastline and the X the start of the ray. Panel b shows the vertical cross-section as interpolated along the ray (black line). The location of the GW packet for this respective time is indicated by the cross of the blue and green lines. The blue line on the left (right) plot shows the horizontal (vertical) wavelength from the backtrace. The green line shows the phase orientation.

to 2.5 hr before the time the WRF model is evaluated. The comparison relies on the assumptions that the GW structure (phase and amplitude) does not alter in this time frame.

The reconstructed GROGRAT GW in Figure 6 compares well to the WRF and ALIMA data. It is noted that the eastern most part of the leg has the biggest time difference between the ALIMA observation and the GROGRAT
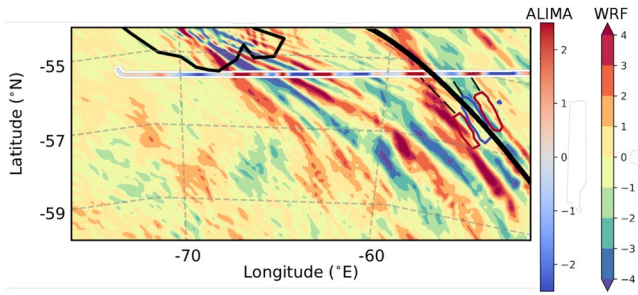
Figure 6. The forward raytrace (bold black line) of the Gimballed Limb Observer for Radiance Imaging of the Atmosphere observed gravity wave (GW) overlaid with WRF and Airborne Lidar for the Middle Atmosphere (ALIMA) data. All data are valid for 27-km altitude. The background data are WRF data while the red and blue lines with the white border represents ALIMA data on the southern flight track after the upward propagating waves were selected with a wavelet transform (Section 2.1.2). The red and blue contour lines are the reconstructed warm and cold phases of the gravity wave (GW) suggested by GROGRAT along the ray path. The GROGRAT reconstructed GW is valid at the respective location and at 27 km. The reconstructed GWs and WRF data are both valid for 12 September 06:00. To guide the eye, the black-dashed lines create a link between GROGRAT reconstruction and the ALIMA track, which shows that the phase fronts of the GW match well. The plot is exclusively used to match the GW structure and validate GROGRAT versus ALIMA. Note that the temperature (in K) scale is different for WRF and ALIMA—the wavelet transform would cause the ALIMA temperature amplitude to be lower than the actual amplitude (Section 2.1.2).

GW; hence, we could expect differences. Between 62° and 68°W, the WRF model and ALIMA compares remarkably well. The WRF data fill the gaps between ALIMA measurements and the reconstructed GROGRAT GW; making it a useful data set. Using the ALIMA data by itself becomes complicated as there are many short horizontal wavelength GWs (e.g., between 62° and 68°W), which is difficult to interpret using only the two ALIMA flight legs. The WRF model simulates the shorter horizontal wavelength GWs well, which makes it easier to interpret the ALIMA data. Another striking feature in Figure 6 is the ray path showing the GWs propagate almost along its phase lines. This is a typical feature of stationary GWs and is discussed in detail in Appendix A of Strube et al. (2021).

3.3. GW Observations: Midstratosphere and Upper Stratosphere

This subsection describes three of the main GW structures observed in the stratosphere. One GW structure proves to be a nonstationary GW and is corrected for in the observations. The corrected nonstationary GW structure reveals refraction at the top of the stratosphere. This refracting GW structure is used in Section 4 to explain how a GW refracts. In this section, GROGRAT shows that the refracting GW propagated up to 2,000 km before being observed by ALIMA. The midstratosphere and upper stratospheric observations were obtained by ALIMA.

ALIMA provides high-resolution 2-D observations above HALO. Normally, a 2-D data set does not allow the determination of the full 3-D GW vector. Thus, on the one hand, a 2-D observation does have a slight disadvantage as opposed to a 3-D data set. But, on the other hand, with creative experiment design (flight planning), this is easily overcome to provide a 3-D wavevector.

To infer also direction information, the racetrack was planned with two parallel flight tracks spaced less than one expected wavelength of the major GW structure. In the following discussion, we use data from 04:15 to 06:05, this implies assuming a stationary environment for ≈2 hr in the combined analysis. We initially assume the GW structure is stationary and test this with every GW packet we observe. The temperature perturbation field shown in Figures 7a and 7b was determined by subtracting a 30 min (corresponding to ~400 km) running mean and applying a wavelet transform as specified in Section 2.1.2.

Three dominant GW families can be identified by eye in Figures 7a and 7b. The southern ALIMA leg (Figure 7a) shows two long horizontal wavelength GWs. A first wavepacket (family 1) has a top at ≈40 km and starts at 32 km—with a weak signature extending down to 27 km (the GWs in Figure 6). Compared to family 1, the phase fronts of the higher wavepacket (family 3) have a steeper slant, show a shorter horizontal wavelength and a smaller GW amplitude. The "dead zone" (weak amplitudes and an incoherent structure) between these packets and the differences in the GW properties indicates that these are two distinct GWs. Horizontal cuts through the ALIMA data (similar to Figure 9) show a well-defined GW pattern that disappears around 40 km. This is further evidence of two GWs rather than structures of the same GW packet.

The northern ALIMA leg (Figure 7b) exhibits three dominant GW packets. Figure 7b show that the first GW packet exhibits strong similarities to family 1 (in the southern leg) in the left plot and is categorized as the same GW packet. Above family 1 (in the "dead zone" of the southern leg in Figure 7a) another GW packet is identified (family 2). The GW packet between 40 and 50 km in Figure 7b has no similarities to family 1 or 3 and is hardly discernible in the southern leg (mainly at flight distances <700 km). This suggests that the GW packet does only weakly extend to the southern leg. With only one leg we cannot determine a 3-D wavevector for family 2. The separation between family 2 and the upper GW packet is around 50 km. The upper GW packet is clearly defined between 51 and 60 km. This GW packet closely resembles family 3 in the southern leg (left) and is categorized accordingly. The presence of three different families hints toward three different origins.

A first attempt is made at determining the source origins with the simple mountain wave model (Section 2.2.1). Figures 7c and 7d represent the reconstructed temperature fluctuations from the mountain wave model sampled along both legs. Considering the simplifications inherent in the model only a qualitative agreement is expected.
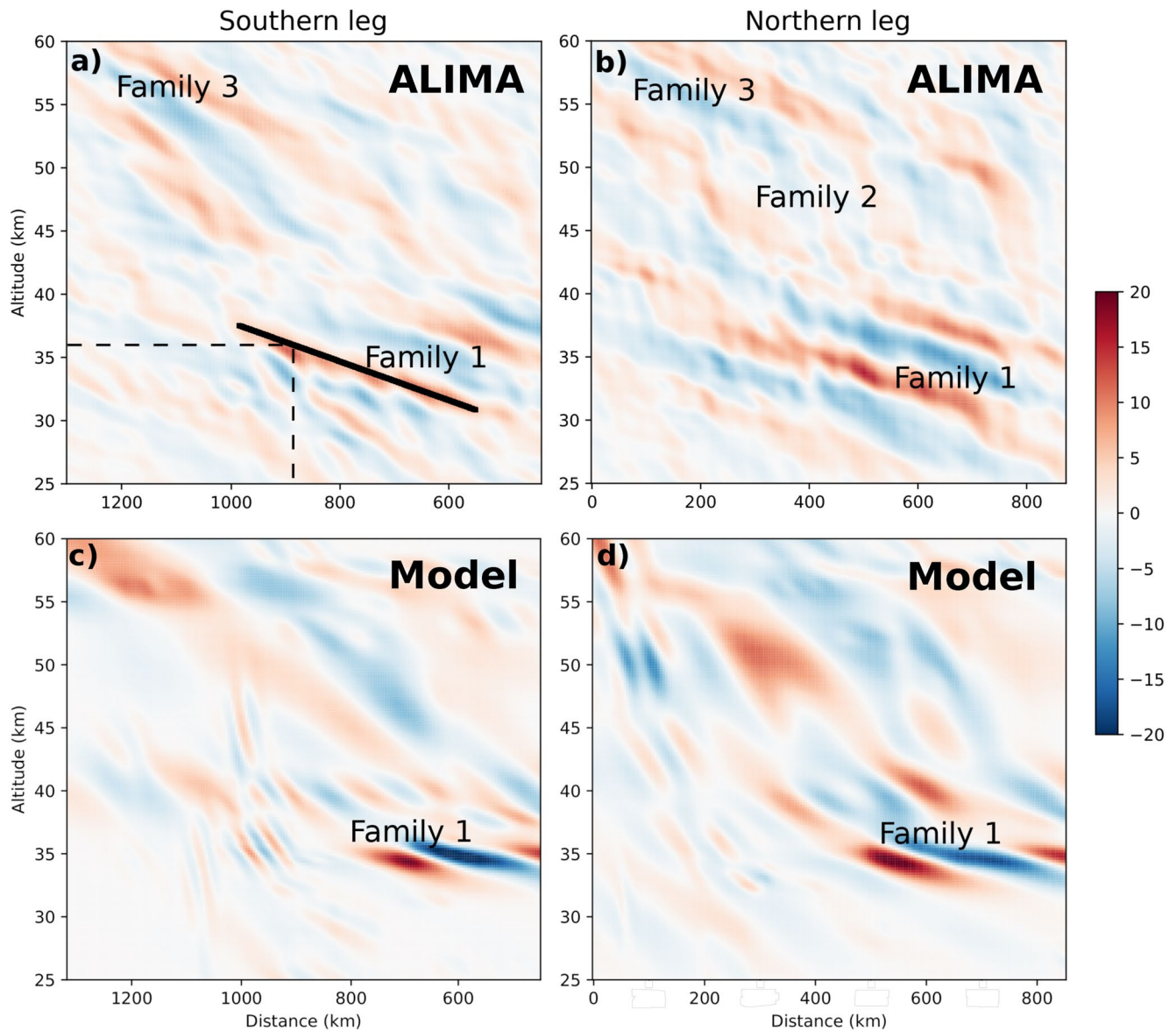
Figure 7. Airborne Lidar for the Middle Atmosphere temperature perturbations (in K) of the southern (a) and northern (b) legs. This is compared to the temperature perturbation from the mountain wave model of the same legs (c—southern leg and d—northern leg). Plots c and d are valid for 05:00. The *x*-axis is distance from the start of the respective flight leg. The eastern part of the southern leg is not shown here in order to have the same distance scale as the northern leg. Plots a and b show westward tilted GW phase fronts only (i.e., upward and westward propagating GWs, see Section 2.1.2). Note the three distinctly different wave packets, here named families 1, 2, and 3. Plots c and d do not see the same GWs for families 2 and 3 (see text for details). The solid and dashed lines indicate the method of determining phase orientation on horizontal plots, see text for details.

The results compare well to ALIMA observations (Figures 7a and 7b) of family 1. The horizontal wavelength is visibly shorter in the mountain wave model. One possible explanation for this is that the mountain wave model only uses the width of the ridge to determine the horizontal wavelength and does not take the low-level blocking width into account as suggested by Geldenhuys (2022b). An interference GW structure exists (Figure 7d) in the layer containing family 2 and only vaguely similar to the ALIMA observations. At first, a structure similar to family 3 is observed in Figures 7c and 7d. However, closer inspection reveals a longer vertical wavelength (7.5 km in ALIMA data and up to 11.3 km in the mountain wave model) and a slower ground-based phase speed (24 m s^{-1} for the ALIMA GW and $\approx$2 m s^{-1} for the mountain wave model GW). Other minor differences include the separation occurring at 43 and 53 km compared to 40 and 50 km in the observations (Figure 7). However, the strong change in phase slant and horizontal wavelength (Figure 7) above and below the separation compare well
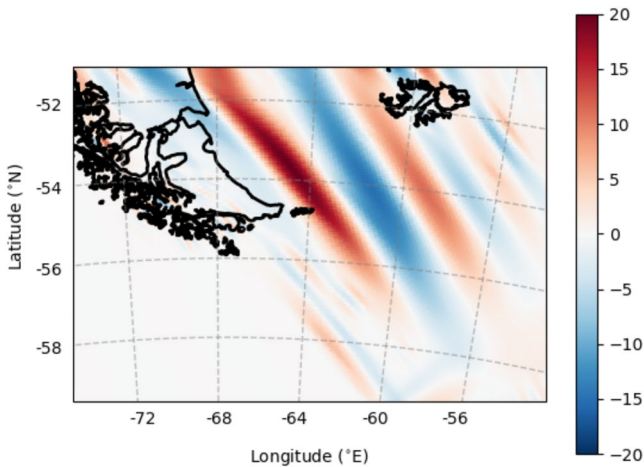
Figure 8. A horizontal cut at 34 km through temperature perturbation (in K) from family 1 as represented by the mountain wave model. Note how far the mountain waves propagate westwards and southwards into the Drake Passage. From this it is clear that gravity waves (GWs) from topographic origin do propagate southwards into the Drake Passage.

between model and observations (Figure 7). The mountain wave model is a linear model and the critical layer at ≈38 km (see the GW momentum deposit discussion in Section 4.2) implies nonlinearity for all GWs above this layer; and provides a possible reason for the mismatch above this layer.

Topography is the only GW source in the model indicating that family 1 stems from the Andes. Figure 8 shows the family 1 GW propagating westwards and southwards in a horizontal cut from the mountain wave model. The mountain waves propagate a significant distance from the mountains demonstrating that source attribution due to colocation is not a good approach. The GW propagating into the Drake Passage is also a possible explanation for the missing GW drag at 60°S. Further analysis into the model showed family 1 originates from the main Andes ridge at 49°S and the incoherent GWs between 40 and 50 km (Figures 7c and 7d) originate from ridges north of 49°S.

3.3.1. ALIMA: GW Family 1

Family 1 is clearly distinguished between 32 and 40 km on both legs (Figures 7a and 7b). From a single 2-D observation, we can obtain a vertical wavelength, but not an accurate horizontal wavelength and no orientation. Comparing the latitude/longitude locations of the same altitude ALIMA temperature perturbations between the two flight segments (e.g., Figure 9) forms a 3-D picture where these can be determined. Phase fronts were approximated linearly in the vertical cut by drawing lines along the phase fronts (e.g., between 32 and 38 km to identify the GWs—solid black line in Figure 7a). Where the fitted line crossed a respective altitude the longitude was noted (dashed line Figure 7a) and marked on the corresponding leg in the horizontal plot (Figure 9). The phase orientation was obtained by connecting these longitudes, forming the phase fronts in Figures 9 and 11. By using this method, we have a more complete picture. The racetrack flight pattern hence allows the determination of an accurate horizontal wavelength and orientation from ALIMA data exclusively.

Figure 9 shows a dominant long horizontal wavelength GW observed by ALIMA. For illustration one cold and warm phase front of the GW packet is drawn in. The blue and red phase fronts of both legs show a wavevector that points to the southwest (250°—measured on the drawn phase fronts). Figure 9 reveals the horizontal wavelength to be 473 km. Using ALIMA data that did not undergo the wavelet transform the amplitude is determined as 15 K. Horizontal cuts at multiple altitudes (seconded by the vertical cuts) show a vertical wavelength of 7.7 km. The ground-based phase speed is calculated using the dispersion relation (Equation 1) and reveal a nearly stationary GW, which is common for mountain waves. This means that we can safely assume the GW remained stationary in time and space in the horizontal over the two flight legs for family 1.

At least two pieces of evidence should be used to confirm the diagnosis of a GW source (e.g., Geldenhuys et al., 2021). The first piece of evidence is the mountain wave model showing approximately the same GW as in the observations (shown in Figures 7c and 7d), implying it is a mountain wave. To confirm this the 3-D wavevector of family 1 was backtraced with GROGRAT to the Andes. Figure 10 show the GW was raytraced to above the main Andes ridge close to the end of the ray. The ray traced from 36 km to directly above the Andes main ridge at ≈52°S. Combining the results from the mountain wave model and GROGRAT, we have confidence the source of family 1 is indeed the Andes main ridge.

3.3.2. ALIMA: GW Family 3

Family 3 exists between 51 and 60 km in Figures 7a and 7b. Figure 11 shows a clear westward slant of phase fronts with altitude between 53 and 55.5 km. Figures 7 and 11 indicate a GW with a vertical wavelength of 7.5 km. Raw temperature residual data (before applying the 2-D Morlet continuous wavelet transform) show an amplitude of 7 K. The dashed phase fronts suggest an initial orientation of 282° and a horizontal wavelength of 291 km.

The dashed phase fronts in Figure 11 form a curious Y-shape pattern with phase lines from the three fronts meeting around 58°S. The most likely explanation is that the GW is not stationary and the phase propagation
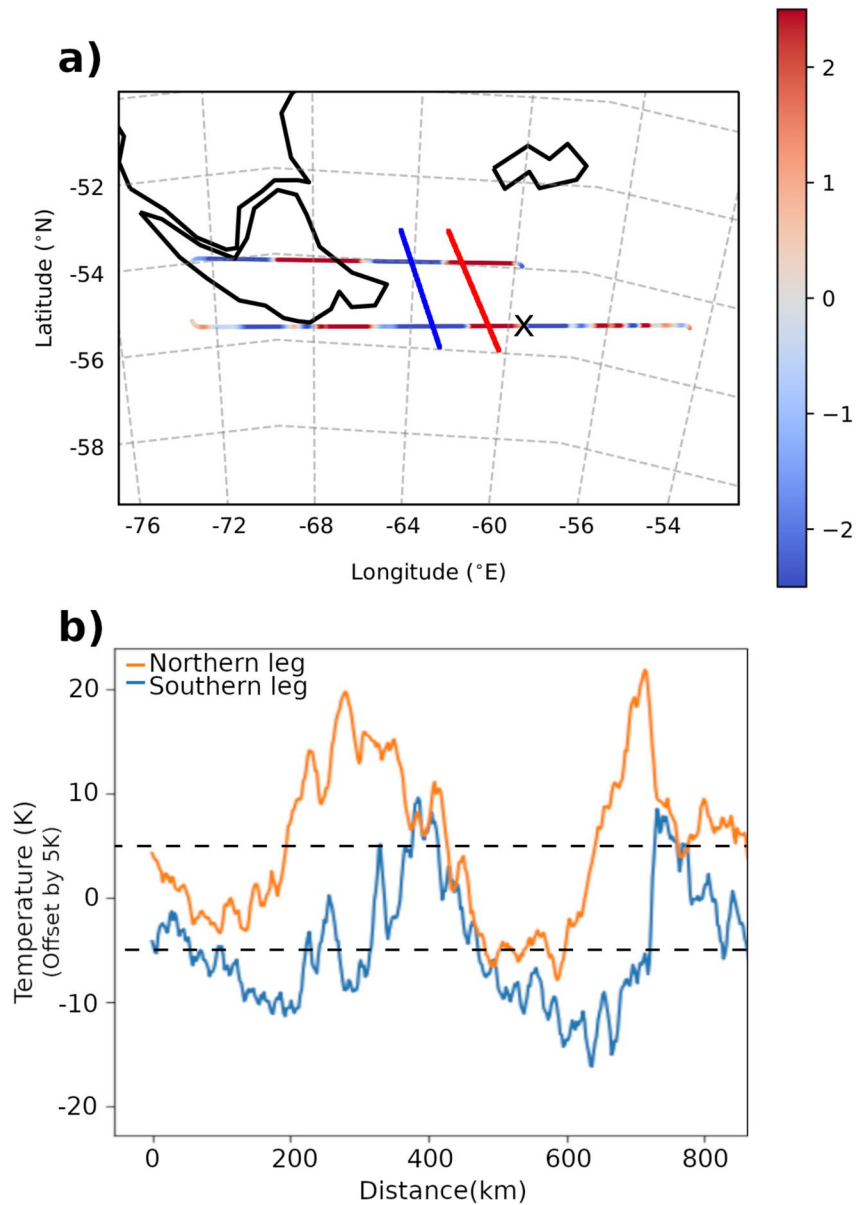
Figure 9. Temperature perturbation (in K) at 36 km as observed by Airborne Lidar for the Middle Atmosphere (ALIMA). (a) Temperature perturbation showing the upward propagating gravity wave (GW) component. In an attempt to mask out short wavelength GWs, a color scale is chosen where the temperature amplitude saturates at 2.5 K. (b) Line plots showing the full temperature perturbation (after 30 min running mean removal) of the northern (orange) and southern (blue) legs. Note that the temperature perturbation is offset by +5 K for the northern and −5 K for the southern legs to improve readability. The southern leg line plot only use data west of the "X" on panel (a) Combining the northern and the southern legs and focusing on the long horizontal wavelength GWs, we can now form a 3-D picture. The drawn in phase fronts were determined with the help of vertical cuts (for an example see the solid line in Figure 7 and corresponding text). For the first time, ALIMA data are used exclusively to determine GW phase orientation. From west to east, we see two full wavelengths starting with a cold phase front.

is to the east. This would stretch the wavelength on the northern leg and shorten it on the southern leg similar to a Doppler shift effect between phase velocity and aircraft movement. The GW has a nonzero ground-based phase speed. To correct for the nonstationarity, we follow an iterative approach of determining the wavelength and phase speed, correcting for the phase speed and determining a new wavelength. We explain this for 53 km as an example in Figure 11 top. Combining the fact that this is an upward propagating GW (see Section 2.1.2) and the westward phase slant with height (Figures 7a and 7b, and 11) as well as the wind direction we know the

GW wave vector points in an approximate westwards direction. To calculate the ground-based phase speed in the x-direction, we need meridional wavenumber l (0 m^{-1}), zonal wavenumber k ($-1.87e-5$ m^{-1} is the average between the two legs; which correspond to a total horizontal wavelength of 336 km), vertical wavenumber m ($8.3e-4$ m^{-1}), stability ($N^2 = 2.276e-4$ s^{-2}), scale height (7,683 m), and zonal wind ($v = 30$ m s^{-1}) obtained from ALIMA observations and ERA5. The calculated intrinsic phase speed in the x-direction is -16.96 m s^{-1}. The zonal wind speed is stronger than the intrinsic phase speed and the GW packet drifts eastwards at 13 m s^{-1} (and 13.1 m s^{-1} at 55.5 km). This means that when observing the warm phase front in the southern leg, the same phase front was located further westward than what it was observed in the northern leg in Figure 11. The phase correction is calculated by

$$\text{correction} = (\text{reference time} - \text{observed time}) \cdot \text{ground-based phase speed} \qquad (6)$$

with a reference time of 05:30. The solid lines between the flight tracks show the corrected phase lines. This correction reduces the Y-shape of the phase fronts and provides a more natural looking GW packet.

The new cold phase fronts (solid blue lines) suggest orientations of 262.8° at 53 km and 270.4° at 55.5 km. Refraction is now evident in the solid phase lines between 53 and 55.5 km in Figure 11. Figure 12 shows that backtracing this new and more accurate 3-D wavevector in GROGRAT reveals the origin of this GW lies upwind of the Andes; another indication of a nonorographic source (the nonstationary GW phase speed being the first). Some weak evidence of a jet generated GW exists; however, conclusive evidence is missing. A peak in WKB values from 0.1 to 0.45 exist where the ray path crosses 24 km—a value of 0.45 is not considered a WKB violation but it is worth noting the peak. (The WKB (Wentzel-Kramers-Brillouin approximation; Hertzog et al., 2001; Marks & Eckermann, 1995) approximation requires the scale of change of the wavenumber is large compared to the wavelength of the GW. Refer to Geldenhuys et al. (2021) and references there in to see how the WKB values and nonorographic GW emission is linked.) No increased values of the cross-stream Lagrangian Rossby number were found in the region. However, an increase in the cross-stream ageostrophic wind was detected at 24.4 km (refer to Geldenhuys et al. (2021) and Zülicke and Peters (2006) for the calculation of these parameters). The cross-stream Lagrangian Rossby and cross-stream ageostrophic wind are an indication when the forces in the jet are not in balance and when spontaneous emission of GWs are possible. In Figure 12b, the ERA5 alternating GW pattern crossing the ray path at 24-km altitude and $-2,000$ km distance confirms the upwind GW. The GW signal is weak near the WKB peak. Also, between $-2,000$ and $-2,200$ km and directly above the ray path a weak V-shaped structure is identified. For waves propagating in the same horizontal direction, the opposite phase tilt of these regions surrounding a central altitude (meaning a V-shaped GW structure in a distance versus altitude cross-section) suggests a local source location that is radiating upward and downward propagating GWs. At 24 km, the ratio f over $\omega_{intrinsic}$ indicated a low-frequency GW (typical of jet generated GWs). That makes four signals that suggests a jet generated GW. Using a rotary analysis technique, a complementary study of this event, de la Torre et al. (2022) found predominantly downwards propagating GWs upwind of the Andes below 25 km—this would be in agreement with an out of balance jet at ≈24 km. If the jet emitted this GW, this provides a curious case where a GW propagated for ≈1,500–2,000 km just to be observed over a mountain. This highlights the fact that a source cannot simply be determined by pure colocation as already mentioned in Krisch et al. (2020), Geldenhuys et al. (2021), Strube et al. (2021) and GWs undergoing refraction propagate long horizontal distances from their sources and are poorly approximated by 1-D parameterizations.

Evidence also exists for a mountain wave present in this region (Figures 7c and 7d). The mountain wave and the nonorographic GW have very different characteristics suggesting that this is not the same GW packet. This altitude layer is a sensitive region with high gradients where the outcome depends highly on the details of the model atmospheric background and the details of the model. There is also evidence that in this region different sources coalesce. Given that above 40 km the reliability of model data is known to decrease (see Ern et al., 2021; Sakazaki et al., 2018), we have insufficient information to disentangle this completely.
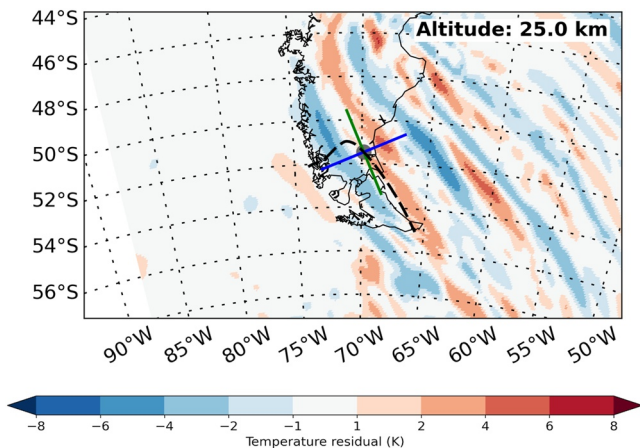

Figure 10. GROGRAT backtracing of Airborne Lidar for the Middle Atmosphere family 1 with ERA5 temperature perturbation (in K) in the background. The green and blue lines are the same as in Figure 5. The fact that this gravity wave (GW) propagates a short horizontal distance while covering 25 km in altitude it hints at a low ground-based phase speed with a long vertical wavelength. Both of these are characteristics of orographic GWs.
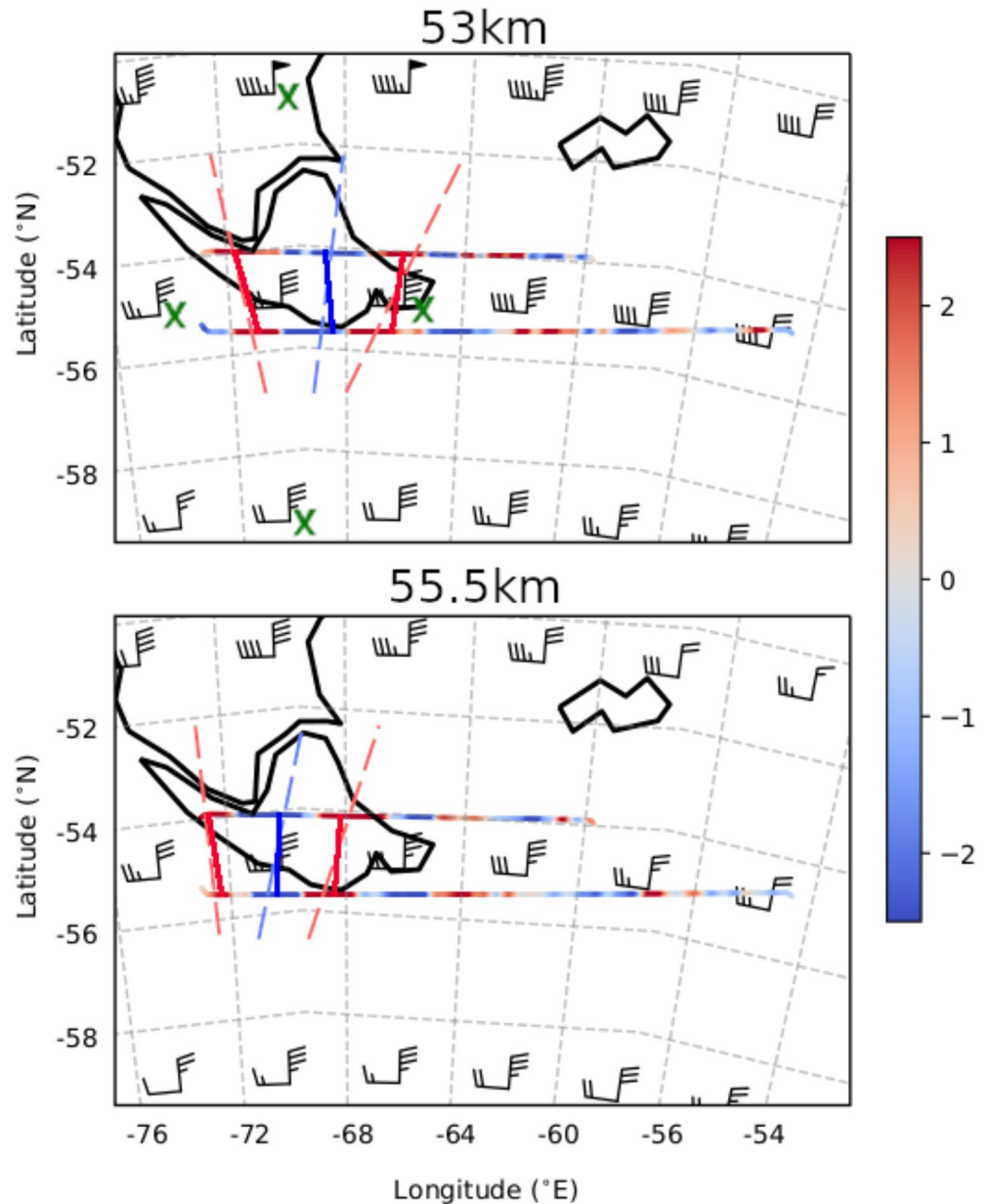
Figure 11. Airborne Lidar for the Middle Atmosphere temperature residuals (in K) showing upward propagating gravity waves (GWs) at 53 and 55.5 km. The background ERA5 zonal and meridional winds are shown in wind barbs. The barbs are similar to Figure 1. Note the winds have a decreasing trend from northwest to southeast and with increasing altitude. The zonal wind speed is also generally weaker than the meridional wind speed. The dashed lines represent the phase fronts as determined from the vertical cut (Section 3.3.1). The dashed phase fronts are then corrected (solid lines connecting the two racetracks) to compensate for GW propagation (see Equation 6 and corresponding text). The green X's on the top plot are used to help diagnose the refraction in Section 4.

4. Refraction: Causality and Consequence

The previous section illustrated GW refraction in the troposphere and the stratosphere. The first subsection uses the background winds (already discussed in the Synoptic discussion of Section 3.1) and the ALIMA observations of refraction to explain how a GW refracts. The second subsection use the refracting GW structure observed by GLORIA (shown in Figure 4) combined with the raytracer to explain the impact of refracting GWs.
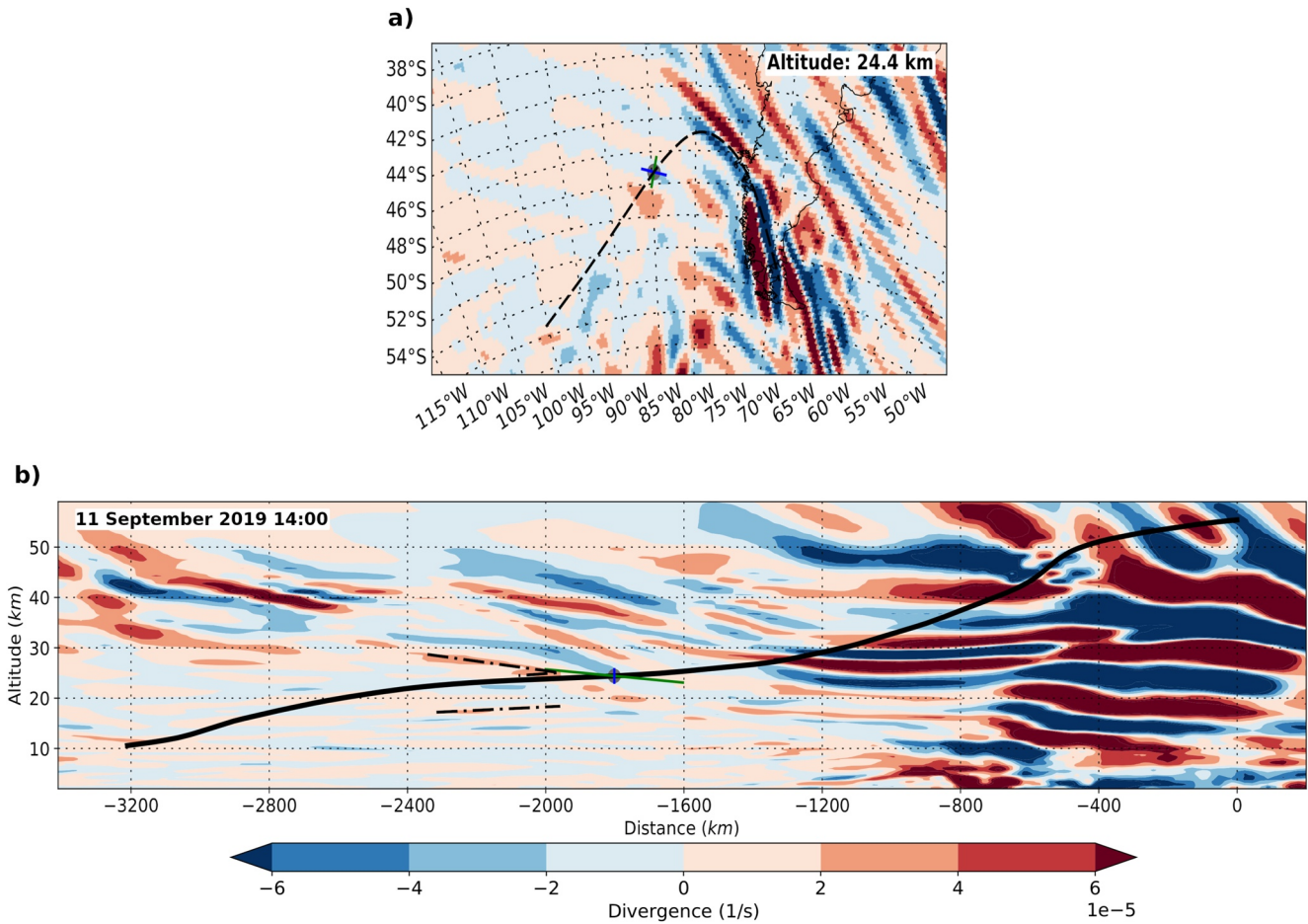
a)

b)

Figure 12. Divergence of ERA5 horizontal winds along the GROGRAT raytrace started at 55.5 km. Both plots are valid for 11 September at 14:00. Panel a shows the horizontal cut at 24.4 km. Panel b shows a vertical cut along the ray path. The dash dot lines show the different phase slants and guide the eye to the weak V-shape pattern (see text for details). The black, blue, and green lines are similar to Figure 5. It is important to note that GROGRAT cannot directly diagnose sources along the ray path and this is left to the user to interpret. That means the source can be located at any point along the ray path, which in this instance, the most likely location is 24 km (see text for details).

4.1. How do GWs Refract?

This section will briefly explain how the GWs refract using the case of family 3. This section does not intend to provide an exact solution of refraction, but rather to describe its general behavior. Horizontal wavelength and wave direction (which depends on the wavelength in the x-direction and y-direction) of a GW change in the presence of a horizontal wind gradient (e.g., Ehard et al., 2017). This is described by Equations 2 and 3 from Lighthill (1978) (also in Marks and Eckermann (1995)). In the presence of strong horizontal wind gradients, the first two terms in Equations 2 and 3 are the dominant ones. We therefore neglect the smaller terms to obtain

$$\frac{dk}{dt} = -k\frac{\partial u}{\partial x} - l\frac{\partial v}{\partial x} \tag{7}$$

$$\frac{dl}{dt} = -k\frac{\partial u}{\partial y} - l\frac{\partial v}{\partial y} \tag{8}$$

Family 3 experiences a significant amount of shear on the edge of the polar vortex and serves as a good example to understand refraction from both theory and observation. In Figure 11, the wind barbs represent ERA5 background zonal and meridional winds without the GW perturbation. The center of the displaced and elongated vortex (shown in Figure 2) is located to the south and results in a decreasing wind speed from northwest to southeast, which is observed in Figure 11. This horizontal shear creates favorable conditions for refraction. Using the winds as input into Equations 7 and 8 we can predict the refraction in time.

Table 1
Parameters for Input Into Equations 7 and 8 Determined From Figure 11

Altitude (km)	∂u in x (m s^{-1})	∂v in x (m s^{-1})	∂u in y (m s^{-1})	∂v in y (m s^{-1})
53	−10	−10	25	15
55.5	−5	−5	25	5

Note. The distances in ∂x and ∂y are 535.1 and 889.6 km, respectively.

The wind gradient is determined in the *x*-direction and *y*-direction between the green X's in Figure 11. The gradients in the *x*-direction are negative (Table 1) while being positive in the *y*-direction. Under normal nondisplaced vortex conditions, one would expect no gradient in the *x*-direction and a positive gradient in the *y*-direction. By placing these gradients together with the wavenumber *k* (calculated from new solid phase lines −1.93e−5 m^{-1}) and *l* (−2.44e−6 m^{-1}; which correspond to a total horizontal wavelength of 223 km) into Equations 7 and 8 we can approximate the derivative *dk/dt* and *dl/dt* as $\Delta k/\Delta t$ and $\Delta l/\Delta t$ (documented in Table 2). Under the assumption that we see the same GW packet, Δt can be estimated from the time it takes the GW to propagate from 53 to 55.5 km; which is 1 hr. The vertical phase speed varies between 0.5 m s^{-1} (1.8 km hr^{-1}) to 0.75 m s^{-1} (2.7 km hr^{-1}) for this GW. For convenience, we assume it at 2.5 km hr^{-1}. According to the resultant Δk and Δl, the total horizontal GW wavelength from 53 to 55.5 km will reduce from 323 to 303 km. The predicted change in angle of orientation is from 262.8° at 53 km to 269.1° at 55.5 km. This compares remarkably well with the 270.4° we observe between the solid phase lines in Figure 11 and the related discussion in Section 3.3.2. The GW is expected to refract by another 5° from 55.5 to 60 km. After the phase correction applied in the previous section (see Figure 11), the ALIMA observations can serve as an example for refraction.

From this section, it is evident that refraction greatly depends on the wavelength and the wind gradient. The wind shear experienced during this flight was anomalously strong for this time of the year. This was caused by the displaced vortex and sudden stratospheric warming (see Section 3.1 and Figure 2), which created a situation better than most to study refraction.

4.2. What Is the Impact of the Refracting GWs?

In this section, we discuss how refraction impacts the atmosphere through taking up additional GWMF and by modifying the propagation path of the GW. Six GROGRAT experiments are conducted to illustrate this. All six experiments use the GW characteristics at the source of the GLORIA observed GW (obtained by backtracing—Section 3.2.3). The forward raytracing experiment starts directly above the source at 4 km (see Figure 13 for the starting location). At the start, the ray the zonal wavenumber was −2.98e−5 m^{-1}, the meridional wavenumber was −1.77e−5 m^{-1}, and the ground-based frequency was −4.57e−4 s^{-1}.

The first experiment (ray #0) is the control experiment and is used to compare to different scenarios. Ray #0 represents the most accurate physics and should be the closest to reality. This entails the use of 4-D propagation setup and a high-resolution background as described in Section 2.3. Figure 13 shows the GW represented by ray #0 rapidly propagates into the stratosphere in a south-eastward direction. Ray #1 uses the same setup but with an enhanced wind gradient in a stronger background flow. The enhanced gradient was obtained by multiplying the background wind with a factor of 1.5. Ray #2 represents the 1-D column parameterization scheme employed by models. This ray can only propagate in the vertical and cannot undergo refraction. Ray #3 is used to reproduce the experiment of Hasha et al. (2008). Hasha et al. (2008) used 3-D raytracing with low-resolution model background data. Input of GW characteristics was determined by a model parameterization scheme. They found that there is no noteworthy reason to include refraction and horizontal propagation of midfrequency GWs into models. Ray #4 uses the exact same settings as ray #3; however, it uses winds from a nonsudden-stratospheric-warming year of 2018. Ray #5 is an attempt at separating the effect of refraction and advection on the location of deposition. Ray #5 uses 4-D propagation settings with a westerly wind with no horizontal gradient. This was achieved by setting the *v*-component to zero and by making the *u*-component a constant wind for every altitude. For every altitude, the *u*-component of the starting location was used to create a constant wind throughout the respective altitude layer. Sato et al. (2012) stated that a strong wind perpendicular to the wave vector will induce leeward drift of the GW. As the GW drifts in the horizontal, it encounters new wind gradients and will adjust/refract to these new conditions. All of the rays, with exception of ray #2, show leeward energy propagation, while all of rays except rays #2 and #5 can refract.

Richard Feynman said that proper experiment design requires you to first reproduce the results from previous work before you can build on that (Leighton & Feynman, 1985). With this in mind the experiment of Hasha

Table 2
Calculated Values to Predict the New Orientation Using Equations 7 and 8 With Values Stated in Table 1

Altitude (km)	$\frac{\Delta k}{\Delta t}$ (m^{-1} s^{-1})	$\frac{\Delta l}{\Delta t}$ (m^{-1} s^{-1})	Δk (m^{-1} s^{-1})	Δl (m^{-1})	Predicted orientation (°)
53	−4.06e−7	5.84e−7	−1.46e−6	2.1e−6	269.1
55.5	−2.03e−7	5.56e−7	−7.31e−7	2.0e−6	274.4

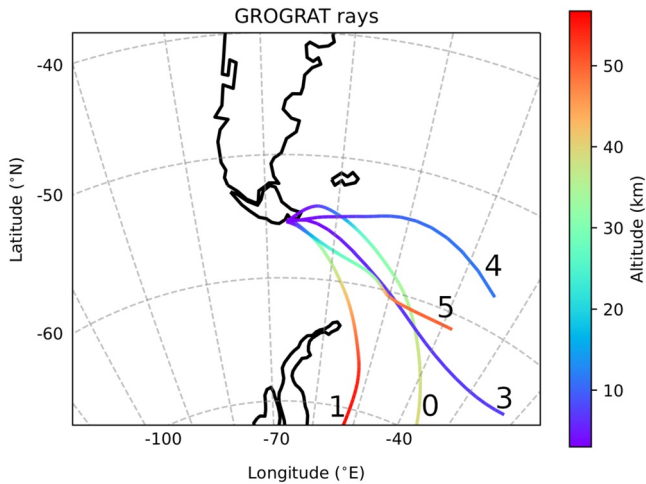*Note*. Wavenumbers *k* and *l* are −1.93e−5 m^{-1} and −2.44e−6 m^{-1} at 53 km.

Figure 13. GROGRAT experiments during forward tracing of the Gimballed Limb Observer for Radiance Imaging of the Atmosphere observed gravity wave (GW; shown in Figures 3 and 4). Ray #0 shows raytracing using the "normal" setup with 4-D propagation in a high-resolution background. Ray #1 uses the same 4-D propagation setup but uses a background u and v wind, which was multiplied by a factor of 1.5. Ray #2 is not depicted here as it will only show as a dot above the starting location. Ray #3 attempts to reproduce the results of Hasha et al. (2008) and uses a coarse resolution background and only 3-D propagation setup. Ray #4 uses the exact same settings as ray #3 but use background conditions of the "normal" year 2018. Ray #5 uses 4-D propagation settings, but with only a westerly wind with no horizontal gradient. Ray #5 is an attempt to separate the effect of advection from refraction.

et al. (2008) was reproduced as closely as possible, but keeping it comparable to the results in this study. To keep the results comparable, the same (as rays #0 to #2) background conditions and ray initial conditions were used (which is a midfrequency GW). Only the GROGRAT setup was changed to represent the 2008 experiment. Ray #3 in Figure 13 was raytraced with the 3-D propagation setup (Section 2.3) in a coarse resolution background. Analogous to the Hasha et al. (2008) experiment the background consisted of a vertical (horizontal) resolution of 1.3 km (2.5°). The resulting forward raytrace of ray #3 follows the same horizontal trajectory as ray #0 at first but diverges toward the end of the ray. Ray #3 remains in the troposphere and at a much lower latitude than ray #0 (which ends at 75°S). Compared to the control ray (ray #0), the relative error in ray #3 is 10° of latitude and 35 km in altitude. The incorrect location of GWMF deposition by ray #3 will result in a noteworthy difference compared to ray #0. More importantly, the results from Hasha et al. (2008) are not reproduced as the GWMF deposit takes place at a significantly lower latitude. With the anomalously different wind regime of 2019, we cannot come to the same conclusion as Hasha et al. (2008).

In another attempt to reproduce the results of Hasha et al. (2008), we used background conditions of a "normal" year. In a new experiment, represented by ray #4 in Figure 13, we use the exact same propagation setup and resolution but using the nonstratospheric-warming year of 2018 as background input into GROGRAT. On 4 September 2018 at 06:00 a similar (to 11 September 2019), tropospheric synoptic system existed where a cold front brushed over the southern Andes with a ridging high-pressure system behind that. We assume that this synoptic system will result in similar GWs to the GLORIA observed GWs. Raytracing the GW in the 2018 conditions we find after 25 hr of propagation the ray (again) remains in the troposphere, but only deviates by 2° of latitude from its source latitude. The small difference in lati-

tude reflects a similar result to the conclusion of Hasha et al. (2008). Ignoring the incorrect altitude of the ray, we can say that the GW will produce drag at roughly the correct latitude. This experiment correctly reproduces the result of Hasha et al. (2008); horizontal propagation and refraction can be ignored without serious repercussions. However, in different circumstances (like this case of 2019 with a weak and displaced vortex) this does not apply. The two experiments used to reproduce Hasha et al. (2008) confirms the finding of Durran (2009) who stated that the impact of refraction on GWMF is case dependent. Chen et al. (2005) and Durran (2009) found in their idealized numerical study that the GWMF is enhanced in regions of divergence and reduced in regions of convergence.

Ray #2 was restricted to vertical propagation and is not identifiable in Figure 13 (as it is only a dot at the starting location below ray #3). Ray #2 attained a maximum altitude of 42 km (similar to our normal conditions represented by ray #0). The drag deposited from ray #2 will be at the correct altitude, but the incorrect latitude and longitude; a major shortcoming (similar to ray #3).

Ray #1 uses background conditions with a stronger wind and an increased wind gradient. By multiplying the background wind with a factor of 1.5, we obtain a total wind speed more representative to normal (compared to the year 2020) stratospheric polar vortex wind speeds. The multiplication also results in a larger wind gradient. It is known that GWs prefer stronger winds to propagate in (if the wind is not too strong to create a propagation lid). Thus, it is no surprise to see ray #1 reach the highest altitude at 57 km. Ray #1 propagates further south and reaches polar vortex altitudes sooner compared to ray #0. The stronger wind with increased gradient creates an even more perfect setting (compared to ray #0) for GW propagation and refraction.

Ray #5 uses no gradient background wind conditions. This means refraction due to windshear will not take place. The experiment was designed to attempt to separate the effect of refraction and GW advection (sometimes called drift) on the location of drag deposition. Figure 13 shows that the GW propagates south eastwards along its phase lines. This result is expected with a westerly wind and a phase orientation from northwest to southeast (see Appendix A of Strube et al. (2021)). This result is also analogous to the result by Sato et al. (2009) who found GWs focus into the jet. From this experiment, it is clear that no refraction is needed for a GW to drift
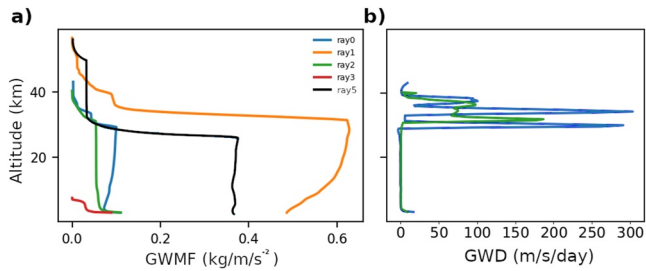
Figure 14. (a) The gravity wave momentum flux (GWMF) along rays #0 to #3 and #5 of the GROGRAT experiment. (b) The GW drag (GWD) along rays #0 and #2. Note the increase in the GWMF along rays #0 and #1, as opposed to rays #2 and #3, which only decrease with altitude. Also note that ray #0 has a lot more GW drag to slowdown the wind compared to ray #2, which has no refraction.

across latitudes, however, compared to rays #0 and #1 refraction does help to propagate further south.

The GWMF of the five rays (excluding the 2018 ray) is compared in Figure 14. The GWMF equation for a single wave (absolute momentum flux Equation 1 from Ern et al. (2015)) is calculated by

$$\text{GWMF} = \frac{1}{2}\rho_0 \frac{\lambda_z}{\lambda_h}\left(\frac{g}{N}\right)^2\left(\frac{\hat{T}}{T}\right)^2 \qquad (9)$$

where λ_z is vertical wavelength and λ_h is horizontal wavelength. Figure 14 shows ray #1 dominates the graph and clearly the stronger wind results in a higher GWMF. GROGRAT takes k, l and ground-based frequency as input and calculates the vertical wavelength from intrinsic phase speed. The intrinsic phase speed is affected by the higher background wind speed, which results in a larger vertical wavelength. This results in an artificial higher GWMF value at the start of rays #1 and #5. Rays #0, #1, #2, and #5 agree somewhat with regards to the altitude where most of the drag is deposited. Ray #3 compares the worst as the ray never reaches the stratosphere. Figure 14 show that ray #0 has a lot more GW drag ($\approx$300 m/s/day) as opposed to ray #2 ($\approx$185 m/s/day) between 30 and 40 km. It is clear that the refracting GW can slow the background wind substantially more (even though they started with the same amount of momentum flux). It is noted that the increase in momentum flux during refraction will accelerate the background wind in the lower levels and slow it more in the upper levels upon deposition (above 30 km in Figure 14). The comparison of the GWMF and GW drag makes it clear that not only the deposition location differs (as described in the first part of this subsection), but also the amount of GWMF and GW drag. Almost all GW parameterizations only consider GWMF decreasing with altitude (e.g., ECMWF, 2015). Rays #2, #3, and #5 follow this assumption, but rays #0 and #1 do not. Figure 15 shows only ray #0 in order to investigate this increase in GWMF.

The GWMF of ray #0 illustrated in Figure 15 shows a clear increase between 4 and 30 km. A strong decrease of horizontal wavelength corresponds with these altitudes. In Section 3, we established that refraction is directly linked to the wavelength of the GW (and in turn the wavelength is linked to the wind gradient). Figure 15 confirms the link between GWMF and horizontal wavelength and therefore suggest a link to refraction. To understand this, we look at the GWMF equation for a single wave, Equation 9. The GWMF equation depends on the horizontal wavelength in the denominator. This means that if the horizontal wavelength decreases (Figure 15, right) the GWMF increases (Figure 15, left). Similarly, in an idealized numerical study Chen et al. (2005) found that the GW wavelength decreases if it propagates through wind divergent regions, increasing the GWMF of the GW. This finding remained valid looking at a single wave and at the total GW packet.

The change in wavelength (hence refraction) makes a significant contribution to the total GWMF of the GW packet. The GWMF along ray #0 increase by as much as 25.7% (scaled by the amount at forcing altitude). Accordingly, ray #0 can deposit a 1/4 more momentum and have a stronger effect on the background flow. The GWMF of ray #1 increases by 30% along the ray. This shows that a stronger wind with a larger wind gradient will account for a greater amount of the GW drag missing from climate models. In a numerical study (on the same date) (Alexander et al., 2022) found a general increase in average GWMF with altitude calculated zonally in the rectangle defined by 45°S 63°W and 60°S 77°W. Similar to Figure 15, they found a general increase with a peak in the GWMF at $\approx$30 km. This can be an indication that all the GWs in this region refract similarly with an increase in GWMF.

It is possible that the increase in GWMF averages out in time with all the other cases where GWMF decreases as a result of refraction (Durran, 2009). This can mean that this process does not have a meaningful impact over a longer time scale; however, this still needs to be confirmed. Kogure et al. (2018) found a year-to-year variation in the GW activity over the Antarctic stratosphere, which they attributed to "probably due to refraction." Even if the GWMF does average out over a time period, it can still have an impact
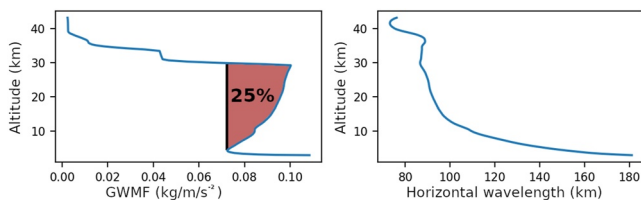

Figure 15. The gravity wave momentum flux (GWMF) and horizontal wavelength along ray #0 of the GROGRAT experiment. Note the maximum change in horizontal wavelength corresponds to the GWMF increase between 4 and 30 km. An increase of 25.7% is observed.

on local dynamics. Literature state that short but sustained bursts of GW activity can have marked impact on dynamics—e.g., Samtleben et al. (2020) found it can help to generate a sudden stratospheric warming. This would mean a few days with an increased amount of GWMF can have an important impact.

The six experiments (five rays plus the repeated Hasha experiment) discussed in this section bring the importance of refraction (and horizontal propagation) forward. Not only do these processes affect where the GWMF is deposited, they also affect the amount of GWMF deposition.

5. Summary

This article provides the first detailed and compelling analysis of GW refraction using high-resolution observations during a sudden stratospheric warming (shown in Figure 2). The reader is to keep in mind that the sudden stratospheric warming resulted in winds that are not representative of the normal this time of year. This article builds on previous studies like Ehard et al. (2017) by providing high-resolution observations of the process of refraction, explaining this with the equations available in literature and by showing through raytracing experiments the impacts of refraction on GWMF. Observations were obtained on 12 September 2019 during the South-TRAC campaign with the airborne GLORIA infrared limb imager and the ALIMA Rayleigh lidar. GLORIA observes the GWs below (shown in Figures 3 and 4) and ALIMA (shown in Figures 7, 9, and 11) above flight altitude. The GLORIA retrieval used the CO_2 lines (936.8–938.6, 939.2–941.0, and 942.2–944 cm^{-1}) to create a 1-D retrieval and a 3-D data set. The observed GW characteristics combined with the GROGRAT raytracer reveal the source of the GW observed by GLORIA is the mountains on the south coast of Patagonia (shown in Figure 5). Tracing the GWs forward produce an excellent match between the GROGRAT reconstructed GWs, high-resolution WRF (3 km in the horizontal and 0.5 km in the vertical—Weather Research and Forecasting model) data and the ALIMA observed GWs (shown in Figure 6). This acts as direct and high-resolution verification of GROGRAT versus observation and model. GLORIA 1-D data show refraction of 16° between 8 and 12 km. The GLORIA 1-D orientation at 8 km is also validated with satellite data, which show an orientation of ≈240° between ≈4 and ≈8 km.

ALIMA 2-D fields reveal three distinctly different GW families (shown in Figures 7a and 7b). The ALIMA retrievals are 2-D data sets, but through creative flight planning (flight track/experimental design) a 3-D data set is obtained. By flying a racetrack (containing two parallel legs) the data from both legs are combined. For the first time, this allowed an accurate horizontal wavelength and orientation observation from lidar measurements—allowing high-resolution refraction studies for GWs that remain stationary across both flight legs. For a nonstationary GWs, such an analysis is still possible if the phase fronts are corrected for any horizontal propagation that occurred between the two legs.

However, this is only valid if the GW remains stationary across the two legs. The dispersion relation combined with the 3-D wavevector shows that family 1 is stationary in the horizontal and family 3 is drifting downstream (eastwards) with time. The second GW family is only observed in the northern flight leg and thus no 3-D wavevector can be determined. To determine an accurate orientation of family 3, the phase fronts are corrected for horizontal propagation (Figure 11). The newly available 3-D wavevector of two of the three wave families is used in GROGRAT to raytrace the GWs. Family 1 traces backwards to the main Andes ridge at 52°S. Family 3 traces backwards upstream of South America and has likely a nonorographic source (shown in Figure 12). A mountain wave model indeed reproduced family 1 of the three GW families and two GW critical layers (Figures 7c and 7d). The model proved to be a great tool to pin point the location of topographical sources. The model only considers mountain waves and thus proposes the source of family 1 is orography. The mountain wave model also illustrated that mountain waves can propagate a substantial distance from their source and into the Drake Passage. This highlights the fact that mountain waves contribute to the 60°S problem.

Family 3 and ERA5 background winds provide the opportunity to explain refraction in detail (Figure 11). GW refraction occurs when the x-wavelength and y-wavelength components change as the wave propagates. Through the use of Equations 7 and 8, it is shown that refraction depends on a change in wavelength, while the change in wavelength depends on the wind gradient. As an illustration, refraction is correctly predicted from 261° at 53 km to 270° at 55.5 km. The prediction is solely made by using the above-mentioned equations, observed wavelengths, background winds, and the calculated vertical propagation speed (to account for time). It is shown that refraction heavily relies on a background wind gradient.

Refraction makes an important contribution to the amount and the distribution of GWMF. A GW packet propagates roughly along its phase lines, which makes the orientation very important to horizontal propagation. Six GROGRAT experiments are used to illustrate the importance of refraction (shown in Figure 13). The experiments use forward raytracing from directly above the source of the GLORIA observed GW. Figure 13 shows the impact on the location of GWMF deposition based on including or excluding refraction and horizontal propagation. The first experiment (also the control experiment—ray #0) represents the most up to date physics and highest resolution background. Ray #1 shows that a stronger wind with a stronger wind gradient allows the ray to reach higher altitudes, propagate further south and refract more. Ray #2 represents the current 1-D parameterization schemes employed by models. This ray can only propagate in the vertical with no refraction. This ray reproduces GWMF deposition at the correct altitude but with the source latitude being incorrect with an error of 20°. Ray #5 shows that refraction can aid a GW to propagate over more latitudes. Ray #3 is an attempt at reproducing the results of Hasha et al. (2008) who stated that refraction and horizontal propagation can be neglected in models.

Similar to Hasha et al. (2008) ray #3 uses a low resolution and only 3-D propagation setup (the background atmosphere remains constant with time). The results from this ray show that 4-D propagation and a high-resolution background is important when raytracing (Figure 13). Ray #3 propagates in a south-eastward direction and remains in the troposphere (very different from ray #2). The deposition latitude in ray #3 is vastly different from the source latitude. This shows that using the anomalously different sudden stratospheric warming background winds we cannot come to the same conclusion as Hasha et al. (2008). In another attempt to reproduce their experiment the same ray #3 is raytraced in the background winds of 4 September 2018 (forming ray #4). This date represents a "normal" year with tropospheric conditions similar to the flight date of 12 September 2019. The ray in the 2018 background remains in the troposphere and only deviates by 2° of latitude. We conclude that we can successfully reproduce the result of Hasha et al. (2008) and that their conclusion holds in this instance under strong polar vortex conditions. Weak vortex conditions (when the vortex is usually stretched or displaced as in Figure 2) produce strong wind shear, which allows for more refraction and further meridional propagation. This confirms the finding by Durran (2009) who stated the effect of refraction on the GWMF differs from case to case. A shortcoming of this study is that it only uses two (if you count the 2018 raytrace) case studies, ideally this needs to be checked over a longer timeframe and is part of an ongoing study.

Perhaps the most important impact of refraction is revealed by the GWMF along the rays. Figures 14 and 15 show an increase in GWMF along the ray path. The information along ray #0 show that the strongest increase in GWMF coincides with the strongest decrease in horizontal wavelength. The GWMF equation (Equation 9) confirms a link with the horizontal wavelength in the denominator. Ray #0 (#1) reveals a 25.7% (30%) increase in the GWMF along the ray. This is a significant increase and implicates that some nonresolved GWs in the model have a quarter too little GWMF during weak vortex conditions. This can make a sizable contribution to the missing drag identified by McLandress et al. (2012) and Garcia et al. (2017). McLandress et al. (2012) state that "modelers should give serious thought" to account for meridional propagation of GWs in parameterization schemes. This article shows that it is empirical that model parameterization schemes should not only include horizontal propagation, but also refraction physics to improve representation of atmospheric dynamics.

Data Availability Statement

The GLORIA 1-D (with filename: ST08_20190911_GLORIA-FZJ_L1V00.02pre-L2Vmgpre.halodb.nc), GLORIA 3-D (with filename: ST08_20190911_GLORIA-FZJ_L1V03.01pre-L2Vmgpre.halodb.nc), ALIMA (with filename: ST08_20190911a_ALIMA_T2Z900.nc), and the WRF data (used to generate Figure 6) are available at https://doi.org/10.5281/zenodo.6997443 (Geldenhuys, 2022a). ERA5 fields can be obtained from the Copernicus Climate Data Store (Copernicus Climate Change Service, 2017).

References

Alexander, M. J., Geller, M., McLandress, C., Polavarapu, S., Preusse, P., Sassi, F., et al. (2010). Recent developments in gravity-wave effects in climate models and the global distribution of gravity-wave momentum flux from observations and models. *Quarterly Journal of the Royal Meteorological Society*, 136(650), 1103–1124. https://doi.org/10.1002/qj.637

Alexander, P., de la Torre, A., Llamedo, P., Hierro, R., Marcos, T., Kaifler, B., et al. (2022). The coexistence of gravity waves from diverse sources during a SouthTRAC flight. *Earth and Space Science Open Archive*, 52. https://doi.org/10.1002/essoar.10511611.1

Amante, C., & Eakins, B. (2009). *ETOPO1 1 arc-minute global relief model: Procedures, data sources and analysis*. National Centers for Environmental Information, NESDIS, NOAA, U.S. Department of Commerce. https://doi.org/10.7289/V5C8276M

Bacmeister, J., Newman, P., Gary, B., & Chan, K. (1994). An algorithm for forecasting mountain wave-related turbulence in the stratosphere. *Weather and Forecasting*, *9*(2), 241–253. https://doi.org/10.1175/1520-0434(1994)009⟨0241:AAFFMW⟩2.0.CO;2

Bauer, R., Grooß, J.-U., Ungermann, J., Bär, M., Geldenhuys, M., & Hoffmann, L. (2022). The Mission Support System (MSS v7.0.0) and its use in planning for the SouthTRAC aircraft campaign. *Geoscientific Model Development Discussions*, *15*, 8983–8997. https://doi.org/10.5194/gmd-2022-155

Boeloeni, G., Kim, Y.-H., Borchert, S., & Achatz, U. (2021). Toward transient subgrid-scale gravity wave representation in atmospheric models. Part I: Propagation model including nondissipative wave-mean-flow interactions. *Journal of the Atmospheric Sciences*, *78*(4), 1317–1338. https://doi.org/10.1175/JAS-D-20-0065.1

Chen, C., & Chu, X. (2017). Two-dimensional Morlet wavelet transform and its application to wave recognition methodology of automatically extracting two-dimensional wave packets from lidar observations in Antarctica. *Journal of Atmospheric and Solar-Terrestrial Physics*, *162*, 28–47. https://doi.org/10.1016/j.jastp.2016.10.016

Chen, C., Durran, D., & Hakim, G. (2005). Mountain-wave momentum flux in an evolving synoptic-scale flow. *Journal of the Atmospheric Sciences*, *62*(9), 3213–3231. https://doi.org/10.1175/JAS3543.1

Copernicus Climate Change Service (C3S). (2017). *ERA5: Fifth generation of ECMWF atmospheric reanalyses of the global climate*. Copernicus Climate Change Service Climate Data Store (CDS). Retrieved from https://cds.climate.copernicus.eu/cdsapp%23%21/home

de la Camara, A., Lott, F., & Hertzog, A. (2014). Intermittency in a stochastic parameterization of nonorographic gravity waves. *Journal of Geophysical Research: Atmospheres*, *119*, 11905–11919. https://doi.org/10.1002/2014JD022002

de la Camara, A., Lott, F., Jewtoukoff, V., Plougonven, R., & Hertzog, A. (2016). On the gravity wave forcing during the southern stratospheric final warming in LMDZ. *Journal of the Atmospheric Sciences*, *73*(8), 3213–3226. https://doi.org/10.1175/JAS-D-15-0377.1

de la Torre, A., Alexander, P., Marcos, T., Hierro, R., Llamedo, P., Hormaechea, J. L., et al. (2022). A spectral rotary analysis of gravity waves: An application during one of the SouthTRAC flights. *Earth and Space Science Open Archive*, *42*. https://doi.org/10.1002/essoar.10512227.1

Doernbrack, A., Eckermann, S. D., Williams, B. P., & Haggerty, J. A. (2021). Stratospheric gravity waves excited by propagating Rossby wave trains. *Journal of the Atmospheric Sciences* (under review). https://doi.org/10.3390/atmos8030049

Dörnbrack, A., Kaifler, B., Kaifler, N., Rapp, M., Wildmann, N., Garhammer, M., et al. (2020). Unusual appearance of mother-of-pearl clouds above El Calafate, Argentina (50°21′S, 72°16′W). *Weather*, *75*(12), 378–388. https://doi.org/10.1002/wea.3863

Dunkerton, T. J. (1984). Inertia gravity waves in the stratosphere. *Journal of the Atmospheric Sciences*, *41*(23), 3396–3404. https://doi.org/10.1175/1520-0469(1984)041<3396:iwits>2.0.co;2

Dunkerton, T. J., & Butchart, N. (1984). Propagation and selective transmission of internal gravity waves in a sudden warming. *Journal of the Atmospheric Sciences*, *41*(8), 1443–1460. https://doi.org/10.1175/1520-0469(1984)041<1443:pastoi>2.0.co;2

Durran, D. (2009). Comments on "gravity wave refraction by three-dimensionally varying winds and the global transport of angular momentum". *Journal of the Atmospheric Sciences*, *66*(7), 2150–2152. https://doi.org/10.1175/2008JAS3013.1

Eckermann, S. D., & Marks, C. J. (1997). GROGRAT: A new model of the global propagation and dissipation of atmospheric gravity waves. *Advances in Space Research*, *20*(6), 1253–1256. https://doi.org/10.1016/s0273-1177(97)00780-1

ECMWF. (2015). *Part IV: Dynamics and numerical procedures*. In *IFS Documentation CY41r1*. ECMWF. https://doi.org/10.21957/p50qmwprw

Ehard, B., Kaifler, B., Dörnbrack, A., Preusse, P., Eckermann, S., Bramberger, M., et al. (2017). Horizontal propagation of large amplitude mountain waves in the vicinity of the polar night jet. *Journal of Geophysical Research: Atmospheres*, *122*, 1423–1436. https://doi.org/10.1002/2016JD025621

Ern, M., Diallo, M., Preusse, P., Mlynczak, M. G., Schwartz, M. J., Wu, Q., & Riese, M. (2021). The semiannual oscillation (SAO) in the tropical middle atmosphere and its gravity wave driving in reanalyses and satellite observations. *Atmospheric Chemistry and Physics*, *21*(18), 13763–13795. https://doi.org/10.5194/acp-21-13763-2021

Ern, M., Hoffmann, L., & Preusse, P. (2017). Directional gravity wave momentum fluxes in the stratosphere derived from high-resolution AIRS temperature data. *Geophysical Research Letters*, *44*, 475–485. https://doi.org/10.1002/2016GL072007

Ern, M., Preusse, P., & Riese, M. (2015). Driving of the SAO by gravity waves as observed from satellite. *Annales Geophysicae*, *33*(4), 483–504. https://doi.org/10.5194/angeo-33-483-2015

Friedl-Vallon, F., Gulde, T., Hase, F., Kleinert, A., Kulessa, T., Maucher, G., et al. (2014). Instrument concept of the imaging Fourier transform spectrometer GLORIA. *Atmospheric Measurement Techniques*, *7*(10), 3565–3577. https://doi.org/10.5194/amt-7-3565-2014

Fritts, D., & Alexander, M. (2003). Gravity wave dynamics and effects in the middle atmosphere. *Reviews of Geophysics*, *41*(1), 1003. https://doi.org/10.1029/2001RG000106

Fritts, D., & Rastogi, P. (1985). Convective and dynamical instabilities due to gravity wave motions in the lower and middle atmosphere: Theory and observations. *Radio Science*, *20*(6), 1247–1277. https://doi.org/10.1029/RS020i006p01247

Garcia, R. R., Smith, A. K., Kinnison, D. E., de la Camara, A., & Murphy, D. J. (2017). Modification of the gravity wave parameterization in the whole atmosphere community climate model: Motivation and results. *Journal of the Atmospheric Sciences*, *74*(1), 275–291. https://doi.org/10.1175/JAS-D-16-0104.1

Gelaro, R., McCarty, W., Suárez, M. J., Todling, R., Molod, A., Takacs, L., et al. (2017). The modern-era retrospective analysis for research and applications, version 2 (MERRA-2). *Journal of Climate*, *30*(14), 5419–5454. https://doi.org/10.1175/JCLI-D-16-0758.1

Geldenhuys, M. (2022a). Dataset for Observations of gravity wave refraction and its causes and consequences. *Zenodo*. https://doi.org/10.5281/zenodo.6997443

Geldenhuys, M. (2022b). On gravity wave parameterisation in vicinity of low-level blocking. *Atmospheric Science Letters*, *23*(6), e1084. https://doi.org/10.1002/asl.1084

Geldenhuys, M., Dyson, L., & van der Mescht, D. (2019). Blocking, gap flow and mountain wave interaction along the coastal escarpment of South Africa. *Theoretical and Applied Climatology*, *139*(3–4), 1291–1303. https://doi.org/10.1007/s00704-019-03030-4

Geldenhuys, M., Preusse, P., Krisch, I., Zülicke, C., Ungermann, J., Ern, M., et al. (2021). Orographically induced spontaneous imbalance within the jet causing a large-scale gravity wave event. *Atmospheric Chemistry and Physics*, *21*(13), 10393–10412. https://doi.org/10.5194/acp-21-10393-2021

Geller, M. A., Alexander, M. J., Love, P. T., Bacmeister, J., Ern, M., Hertzog, A., et al. (2013). A comparison between gravity wave momentum fluxes in observations and climate models. *Journal of Climate*, *26*(17), 6383–6405. https://doi.org/10.1175/JCLI-D-12-00545.1

Gupta, A., Birner, T., Dörnbrack, A., & Polichtchouk, I. (2021). Importance of gravity wave forcing for springtime southern polar vortex breakdown as revealed by ERA5. *Geophysical Research Letters*, *48*, e2021GL092762. https://doi.org/10.1029/2021GL092762

Hasha, A., Bühler, O., & Scinocca, J. (2008). Gravity wave refraction by three-dimensionally varying winds and the global transport of angular momentum. *Journal of the Atmospheric Sciences*, *65*(9), 2892–2906. https://doi.org/10.1175/2007jas2561.1

Haucheorne, A., & Chanin, M. L. (1980). Density and temperature profiles obtained by lidar between 35 and 70 km. *Geophysical Research Letters*, *7*(8), 565–568. https://doi.org/10.1029/GL007i008p00565

Hersbach, H., Bell, B., Berrisford, P., Hirahara, S., Horanyi, A., Munoz-Sabater, J., et al. (2020). The ERA5 global reanalysis. *Quarterly Journal of the Royal Meteorological Society*, *146*(730), 1999–2049. https://doi.org/10.1002/qj.3803

Hertzog, A., Souprayen, C., & Hauchecorne, A. (2001). Observation and backward trajectory of an inertio-gravity wave in the lower stratosphere. *Annales Geophysicae*, *19*(9), 1141–1155. https://doi.org/10.5194/angeo-19-1141-2001

Hindley, N. P., Wright, C. J., Hoffmann, L., Moffat-Griffin, T., & Mitchell, N. J. (2020). An 18-year climatology of directional stratospheric gravity wave momentum flux from 3-D satellite observations. *Geophysical Research Letters*, *47*, e2020GL089557. https://doi.org/10.1029/2020GL089557

Holton, J. R. (2004). *An introduction to dynamic meteorology* (3rd ed.). Academic Press.

Höpfner, M., Ungermann, J., Borrmann, S., Wagner, R., Spang, R., Riese, M., et al. (2019). Ammonium nitrate particles formed in upper troposphere from ground ammonia sources during Asian monsoons. *Nature Geoscience*, *12*(8), 1752–0908. https://doi.org/10.1038/s41561-019-0385-8

ICAO. (2005). *Manual on low-level wind shear*. International Civil Aviation Organization.

Kaifler, B., & Kaifler, N. (2021). A compact Rayleigh autonomous lidar (CORAL) for the middle atmosphere. *Atmospheric Measurement Techniques*, *14*, 1715–1732. https://doi.org/10.5194/amt-14-1715-2021

Kaifler, N., Kaifler, B., Dörnbrack, A., Rapp, M., Hormaechea, J. L., & de la Torre, A. (2020). Lidar observations of large-amplitude mountain waves in the stratosphere above tierra Del Fuego, Argentina. *Nature: Scientific Reports*, *10*(1), 14529. https://doi.org/10.1038/s41598-020-71443-7

Kaifler, N., Kaifler, B., Ehard, B., Gisinger, S., Dornbrack, A., Rapp, M., et al. (2017). Observational indications of downward-propagating gravity waves in middle atmosphere lidar data. *Journal of Atmospheric and Solar-Terrestrial Physics*, *162*(SI), 16–27. https://doi.org/10.1016/j.jastp.2017.03.003

Kaufmann, M., Blank, J., Guggenmoser, T., Ungermann, J., Engel, A., Ern, M., et al. (2015). Retrieval of three-dimensional small-scale structures in upper-tropospheric/lower-stratospheric composition as measured by GLORIA. *Atmospheric Measurement Techniques*, *8*(1), 81–95. https://doi.org/10.5194/amt-8-81-2015

Kidston, J., Scaife, A. A., Hardiman, S. C., Mitchell, D. M., Butchart, N., Baldwin, M. P., & Gray, L. J. (2015). Stratospheric influence on tropospheric jet streams, storm tracks and surface weather. *Nature Geoscience*, *8*(6), 433–440. https://doi.org/10.1038/ngeo2424

Kim, Y.-H., Boeloeni, G., Borchert, S., Chun, H., & Achatz, U. (2021). Toward transient subgrid-scale gravity wave representation in atmospheric models. Part II: Wave intermittency simulated with convective sources. *Journal of the Atmospheric Sciences*, *78*(4), 1339–1357. https://doi.org/10.1175/JAS-D-20-0066.1

Kleinert, A., Friedl-Vallon, F., Guggenmoser, T., Höpfner, M., Neubert, T., Ribalda, R., et al. (2014). Level 0 to 1 processing of the imaging Fourier transform spectrometer GLORIA: Generation of radiometrically and spectrally calibrated spectra. *Atmospheric Measurement Techniques*, *7*(12), 4167–4184. https://doi.org/10.5194/amt-7-4167-2014

Kogure, M., Nakamura, T., Ejiri, M. K., Nishiyama, T., Tomikawa, Y., & Tsutsumi, M. (2018). Effects of horizontal wind structure on a gravity wave event in the middle atmosphere over Syowa (69°S, 40°E), the Antarctic. *Geophysical Research Letters*, *45*, 5151–5157. https://doi.org/10.1029/2018GL078264

Kogure, M., Yue, J., & Liu, H. (2021). Gravity wave weakening during the 2019 Antarctic stratospheric sudden warming. *Geophysical Research Letters*, *48*, e2021GL092537. https://doi.org/10.1029/2021GL092537

Kogure, M., Yue, J., Nakamura, T., Hoffmann, L., Vadas, S. L., Tomikawa, Y., et al. (2020). First direct observational evidence for secondary gravity waves generated by mountain waves over the Andes. *Geophysical Research Letters*, *47*, e2020GL088845. https://doi.org/10.1029/2020GL088845

Kohma, M., Sato, K., Nishimura, K., & Tsutsumi, M. (2021). Weakening of polar mesosphere winter echo and turbulent energy dissipation rates after a stratospheric sudden warming in the southern hemisphere in 2019. *Geophysical Research Letters*, *48*, e2021GL092705. https://doi.org/10.1029/2021GL092705

Krasauskas, L., Ungermann, J., Ensmann, S., Krisch, I., Kretschmer, E., Preusse, P., & Riese, M. (2019). 3-D tomographic limb sounder retrieval techniques: Irregular grids and Laplacian regularisation. *Atmospheric Measurement Techniques*, *12*(2), 853–872. https://doi.org/10.5194/amt-12-853-2019

Krasauskas, L., Ungermann, J., Preusse, P., Friedl-Vallon, F., Zahn, A., Ziereis, H., et al. (2021). 3-D tomographic observations of Rossby wave breaking over the North Atlantic during the wise aircraft campaign in 2017. *Atmospheric Chemistry and Physics*, *21*(13), 10249–10272. https://doi.org/10.5194/acp-21-10249-2021

Jülich Supercomputing Centre. (2018). JURECA: Modular supercomputer at Jülich Supercomputing Centre. *Journal of Large-Scale Research Facilities*, *4*, A132. https://doi.org/10.17815/jlsrf-4-121-1

Krisch, I., Ern, M., Hoffmann, L., Preusse, P., Strube, C., Ungermann, J., et al. (2020). Superposition of gravity waves with different propagation characteristics observed by airborne and space-borne infrared sounders. *Atmospheric Chemistry and Physics*, *20*(19), 11469–11490. https://doi.org/10.5194/acp-20-11469-2020

Krisch, I., Preusse, P., Ungermann, J., Dörnbrack, A., Eckermann, S. D., Ern, M., et al. (2017). First tomographic observations of gravity waves by the infrared limb imager GLORIA. *Atmospheric Chemistry and Physics*, *17*(24), 14937–14953. https://doi.org/10.5194/acp-17-14937-2017

Krisch, I., Ungermann, J., Preusse, P., Kretschmer, E., & Riese, M. (2018). Limited angle tomography of mesoscale gravity waves by the infrared limb-sounder GLORIA. *Atmospheric Measurement Techniques*, *11*(7), 4327–4344. https://doi.org/10.5194/amt-11-4327-2018

Lang, S. T., Dawson, A., Diamantakis, M., Dueben, P., Hatfield, S., Leutbecher, M., et al. (2021). More accuracy with less precision. *Quarterly Journal of the Royal Meteorological Society*, *147*(741), 4358–4370. https://doi.org/10.1002/qj.4181

Leighton, R., & Feynman, R. (1985). *"Surely you're joking, Mr. Feynman!": Adventures of a curious character*. W. W. Norton.

Lighthill, M. J. (1978). *Waves in fluids* (pp. 504). Cambridge University Press.

Lim, E., Hendon, H., Boschat, G., Hudson, D., Thompson, D., Dowdy, A., & Arblaster, J. (2019). Australian hot and dry extremes induced by weakenings of the stratospheric polar vortex. *Nature Geoscience*, *12*(11), 896–901. https://doi.org/10.1038/s41561-019-0456-x

Marks, C. J., & Eckermann, S. D. (1995). A three-dimensional nonhydrostatic ray-tracing model for gravity waves: Formulation and preliminary results for the middle atmosphere. *Journal of the Atmospheric Sciences*, *52*(11), 1959–1984. https://doi.org/10.1175/1520-0469(1995)052⟨1959:ATDNRT⟩2.0.CO;2

McLandress, C. (1998). On the importance of gravity waves in the middle atmosphere and their parameterization in general circulation models. *Journal of Atmospheric and Solar-Terrestrial Physics*, *60*(14), 1357–1383. https://doi.org/10.1016/S1364-6826(98)00061-3

McLandress, C., Shepherd, T. G., Polavarapu, S., & Beagley, S. R. (2012). Is missing orographic gravity wave drag near 60 degrees S the cause of the stratospheric zonal wind biases in chemistry climate models? *Journal of the Atmospheric Sciences*, *69*(3), 802–818. https://doi.org/10.1175/JAS-D-11-0159.1

Pitteway, M. L. V., & Hines, C. O. (1963). The viscous damping of atmospheric gravity waves. *Canadian Journal of Physics*, *41*(12), 1935–1948. https://doi.org/10.1139/p63-194

Plougonven, R., de la Camara, A., Hertzog, A., & Lott, F. (2020). How does knowledge of atmospheric gravity waves guide their parameterizations? *Quarterly Journal of the Royal Meteorological Society*, *146*(728), 1529–1543. https://doi.org/10.1002/qj.3732

Polichtchouk, I., Shepherd, T., & Byrne, N. (2018a). Impact of parametrized nonorographic gravity wave drag on stratosphere-troposphere coupling in the northern and southern hemispheres. *Geophysical Research Letters*, *45*, 8612–8618. https://doi.org/10.1029/2018GL078981

Polichtchouk, I., Shepherd, T., Hogan, R., & Bechtold, P. (2018b). Sensitivity of the Brewer-Dobson circulation and polar vortex variability to parameterized nonorographic gravity wave drag in a high-resolution atmospheric model. *Journal of the Atmospheric Sciences*, *75*(5), 1525–1543. https://doi.org/10.1175/JAS-D-17-0304.1

Preusse, P., Dörnbrack, A., Eckermann, S. D., Riese, M., Schaeler, B., Bacmeister, J. T., et al. (2002). Space-based measurements of stratospheric mountain waves by CRISTA, 1. Sensitivity, analysis method, and a case study. *Journal of Geophysical Research*, *107*(D23), 8178. https://doi.org/10.1029/2001JD000699

Preusse, P., Eckermann, S. D., Ern, M., Oberheide, J., Picard, R. H., Roble, R. G., et al. (2009). Global ray tracing simulations of the SABER gravity wave climatology. *Journal of Geophysical Research*, *114*, D08126. https://doi.org/10.1029/2008JD011214

Rapp, M., Kaifler, B., Dörnbrack, A., Gisinger, S., Mixa, T., Reichert, R., et al. (2021). SouthTRAC-GW: An airborne field campaign to explore gravity wave dynamics at the world's strongest hotspot. *Bulletin of the American Meteorological Society*, *102*(4), E871–E893. https://doi.org/10.1175/BAMS-D-20-0034.1

Reichert, R., Kaifler, B., Kaifler, N., Dörnbrack, A., Rapp, M., & Hormaechea, J. L. (2021). High-cadence lidar observations of middle atmospheric temperature and gravity waves at the southern Andes hot spot. *Journal of Geophysical Research: Atmospheres*, *126*, e2021JD034683. https://doi.org/10.1029/2021JD034683

Reichert, R., Kaifler, B., Kaifler, N., Rapp, M., Pautet, P., Taylor, M., et al. (2019). Retrieval of intrinsic mesospheric gravity wave parameters using lidar and airglow temperature and meteor radar wind data. *Atmospheric Measurement Techniques*, *12*(11), 5997–6015. https://doi.org/10.5194/amt-12-5997-2019

Richter, J. H., Sassi, F., & Garcia, R. R. (2010). Toward a physically based gravity wave source parameterization in a general circulation model. *Journal of the Atmospheric Sciences*, *67*(1), 136–156. https://doi.org/10.1175/2009jas3112.1

Riese, M., Oelhaf, H., Preusse, P., Blank, J., Ern, M., Friedl-Vallon, F., et al. (2014). Gimballed Limb Observer for Radiance Imaging of the Atmosphere (GLORIA) scientific objectives. *Atmospheric Measurement Techniques*, *7*(7), 1915–1928. https://doi.org/10.5194/amt-7-1915-2014

Sakazaki, T., Fujiwara, M., & Shiotani, M. (2018). Representation of solar tides in the stratosphere and lower mesosphere in state-of-the-art reanalyses and in satellite observations. *Atmospheric Chemistry and Physics*, *18*(2), 1437–1456. https://doi.org/10.5194/acp-18-1437-2018

Samtleben, N., Kuchař, A., Šácha, P., Pišoft, P., & Jacobi, C. (2020). Impact of local gravity wave forcing in the lower stratosphere on the polar vortex stability: Effect of longitudinal displacement. *Annales Geophysicae*, *38*(1), 95–108. https://doi.org/10.5194/angeo-38-95-2020

Sandu, I., Bechtold, P., Beljaars, A., Bozzo, A., Pithan, F., Shepherd, T. G., & Zadra, A. (2016). Impacts of parameterized orographic drag on the northern hemisphere winter circulation. *Journal of Advances in Modeling Earth Systems*, *8*, 196–211. https://doi.org/10.1002/2015MS000564

Sato, K., Tateno, S., Watanabe, S., & Kawatani, Y. (2012). Gravity wave characteristics in the southern hemisphere revealed by a high-resolution middle-atmosphere general circulation model. *Journal of the Atmospheric Sciences*, *69*(4), 1378–1396. https://doi.org/10.1175/JAS-D-11-0101.1

Sato, K., Watanabe, S., Kawatani, Y., Tomikawa, Y., Miyazaki, K., & Takahashi, M. (2009). On the origins of mesospheric gravity waves. *Geophysical Research Letters*, *36*, L19801. https://doi.org/10.1029/2009GL039908

Savitzky, A., & Golay, M. J. E. (1964). Smoothing and differentiation of data by simplified least squares procedures. *Analytical Chemistry*, *36*(8), 1627–1639. https://doi.org/10.1021/ac60214a047

Shen, X., Wang, L., & Osprey, S. (2020). Tropospheric forcing of the 2019 Antarctic sudden stratospheric warming. *Geophysical Research Letters*, *47*, e2020GL089343. https://doi.org/10.1029/2020GL089343

Strube, C., Ern, M., Preusse, P., & Riese, M. (2020). Removing spurious inertial instability signals from gravity wave temperature perturbations using spectral filtering methods. *Atmospheric Measurement Techniques*, *13*(9), 4927–4945. https://doi.org/10.5194/amt-13-4927-2020

Strube, C., Preusse, P., Ern, M., & Riese, M. (2021). Propagation paths and source distributions of resolved gravity waves in ECMWF-IFS analysis fields around the southern polar night jet. *Atmospheric Chemistry and Physics*, *21*(24), 18641–18668. https://doi.org/10.5194/acp-21-18641-2021

Torrence, C., & Compo, G. P. (1998). A practical guide to wavelet analysis. *Bulletin of the American Meteorological Society*, *79*(1), 61–78. https://doi.org/10.1175/1520-0477(1998)079⟨0061:APGTWA⟩2.0.CO;2

Ungermann, J., Blank, J., Lotz, J., Leppkes, K., Hoffmann, L., Guggenmoser, T., et al. (2011). A 3-D tomographic retrieval approach with advection compensation for the air-borne limb-imager GLORIA. *Atmospheric Measurement Techniques*, *4*(11), 2509–2529. https://doi.org/10.5194/amt-4-2509-2011

Ungermann, J., Kaufmann, M., Hoffmann, L., Preusse, P., Oelhaf, H., Friedl-Vallon, F., & Riese, M. (2010). Towards a 3-D tomographic retrieval for the air-borne limb-imager GLORIA. *Atmospheric Measurement Techniques*, *3*(6), 1647–1665. https://doi.org/10.5194/amt-3-1647-2010

Vadas, S. L., & Becker, E. (2019). Numerical modeling of the generation of tertiary gravity waves in the mesosphere and thermosphere during strong mountain wave events over the southern Andes. *Journal of Geophysical Research: Space Physics*, *124*, 7687–7718. https://doi.org/10.1029/2019JA026694

Van der Mescht, D., & Geldenhuys, M. (2019). Observations of mountain waves with interference generated by coastal mountains in south Africa. *Meteorological Applications*, *26*(3), 409–415. https://doi.org/10.1002/met.1771

Woiwode, W., Dörnbrack, A., Bramberger, M., Friedl-Vallon, F., Haenel, F., Höpfner, M., et al. (2018). Mesoscale fine structure of a tropopause fold over mountains. *Atmospheric Chemistry and Physics*, *18*(21), 15643–15667. https://doi.org/10.5194/acp-18-15643-2018

Zhu, X. (1993). Radiative damping revisited—Parametrization of damping rate in the middle atmosphere. *Journal of the Atmospheric Sciences*, *50*(17), 3008–3021. https://doi.org/10.1175/1520-0469(1993)050⟨3008:RDRPOD⟩2.0.CO;2

Zülicke, C., & Peters, D. (2006). Simulation of inertia-gravity waves in a poleward-breaking Rossby wave. *Journal of the Atmospheric Sciences*, *63*(12), 3253–3276. https://doi.org/10.1175/JAS3805.1